Author manuscript of article published in *Biomacromolecules* **2024**. DOI: 10.1021/acs.biomac.4c01146

Silk Sericin/Chitosan Supramolecular Multilayered Thin Films as Sustainable Cytocompatible Nanobiomaterials

Miguel Rosas,[1,2] Cristiana F. V. Sousa,[1] Ana Pereira,[1] Adérito J. R. Amaral,[1] Tamagno Pesqueira,[1] Sónia G. Patrício,[1] Sara Fateixa,[1] Helena I. S. Nogueira,[1] João F. Mano,[1] Ana L. Oliveira,[2] and João Borges[1*]*

[1]CICECO – Aveiro Institute of Materials, Department of Chemistry, University of Aveiro, Campus Universitário de Santiago, 3810-193 Aveiro, Portugal

[2]CBQF-Centro de Biotecnologia e Química Fina – Laboratório Associado, Universidade Católica Portuguesa, Escola Superior de Biotecnologia, Rua Diogo Botelho 1327, 4169-005 Porto, Portugal

*Corresponding authors: aloliveira@ucp.pt (A.L.O.), joaoborges@ua.pt (J.B.)

KEYWORDS: Silk sericin; Chitosan; Layer-by-Layer technology; Self-assembled nanobiomaterials; Nanofibrillar matrices; Cytocompatibility

ABSTRACT

Silk sericin (SS) has been widely discarded as a waste by the silk textile industry during the degumming process to obtain fibroin. However, in the last decade, an in-depth understanding of its properties and functions turned it into a high added-value biomaterial for biomedical applications. Herein, we report the molecular design and development of sustainable supramolecular multilayered nanobiomaterials encompassing SS and oppositely charged chitosan (CHT) through combination of self-assembly and electrostatically-driven layer-by-layer (LbL) assembly technology. The successful build-up of SS/CHT multilayered nanobiomaterials was demonstrated by the quartz crystal microbalance with dissipation monitoring and attenuated total reflectance-Fourier transform infrared spectroscopy, and the nanofilms' wettable properties and nanofibrillar-like topography were shown by water contact angle, atomic force microscopy, and scanning electron microscopy. *In vitro* assays demonstrated the cytocompatibility of the LbL nanofilms towards human primary dermal fibroblasts, holding great promise as biofunctional nanocoatings for drug/therapeutics/cell delivery, tissue engineering and regenerative medicine.

INTRODUCTION

Nature provides us with an unprecedented source of structures formed by supramolecular interactions. Among them, the native extracellular matrix (ECM), which is tissue and organ specific and formed by the non-covalent self-assembly of mainly fibrous proteins and proteoglycans, has been boosting the scientific community to develop advanced supramolecular multicomponent biomaterials that could recreate its complex composition, nanofibrous structure and dynamic functional behavior, and be used in tissue engineering and regenerative medicine strategies.[1–3] Natural biopolymers, such as proteins and polysaccharides, have been in the limelight when aiming to develop ECM-mimetic biomaterials owing to their physicochemical, structural and biological properties, including biocompatibility, biodegradability, ease of functionalization, and structural similarity to the ECMs of native tissues.[2,4] However, despite the progress achieved to date, recreating the multiple features of the native ECM remains a major challenge. Natural silk proteins, in particular silk fibroin (SF), extracted mainly from the domesticated mulberry silkworm *Bombyx mori* but also from spiders, has been widely processed into a wide variety of size- and shape-tunable silk-based biomaterials for biomedical applications and the textile industry owing to its biocompatibility, biodegradability, ease of purification, cost-effectiveness, structural integrity and remarkable mechanical properties.[5–8] Those include hydrogels,[9,10] coatings/films/membranes,[11,12] sponges,[13] particles/capsules,[14] among others with applications in drug delivery, as *in vitro* disease models, or as implantable biomaterials.[8,15,16]

The simple, inexpensive and highly versatile bottom-up Layer-by-Layer (LbL) assembly technology has been widely employed to functionalize virtually any type of surface with a wide array of building blocks exhibiting complementary intermolecular interactions,[17–19] and fabricate size- and shape-tunable ECM-mimetic multicomponent assemblies with tailored thickness, composition, structure and functions at the nanoscale for multiple biomedical

applications.[20–24] In particular, biocompatible and biodegradable SF-on-SF multilayered nanofilms have been LbL assembled on solid substrates by mainly hydrophobic interactions, but also by electrostatic interactions to some extent, and used to modulate cell functions.[11,25,26] Furthermore, SF-on-SF thin multilayered particles and hollow microcapsules denoting controlled shell thickness and permeability have been prepared by resorting to hydrogen bonding, stabilized by hydrophobic interactions, and used as drug delivery vehicles.[14] In addition, multilayered thin films encompassing SF and oppositely charged natural polymers, namely chitosan (CHT) and alginate, have been assembled on solid surfaces, under mild conditions, via a combination of hydrogen bonding and electrostatic interactions.[27–30] These multilayered films are attractive biomaterial coatings that could be explored as nanoplatforms for cell culture in a variety of tissue engineering and regenerative medicine scenarios.

However, silk sericin (SS), the other major silk protein component composed mainly of serine, aspartic acid and glycine, which glues SF fibers together to form and ensure the cohesion of the cocoons (represents 25-30% of the silk cocoons), has been traditionally widely discarded as a waste product of silk textile industry during the degumming process to separate SF from SS.[31,32] As such, it poses a major environmental impact and does not make use of SS potential as a high added-value 'greener' protein-rich biomaterial for a wide array of biomedical applications.[31,33–35] Although, in the past, SS was reported to elicit an allergenic and immune response, more recently, it has been demonstrated that SS, on its own, is non-immunogenic and only induces an immune response when combined with SF.[31,35–38] In fact, in the last decade, we have witnessed an increase in the number of studies reporting the use of SS as a sustainable and highly attractive biomaterial for addressing various biomedical applications owing to its excellent biocompatibility, biodegradability, wide and readily availability, hydrophilic nature, antibacterial, antioxidant and antimicrobial properties and intrinsic ability to promote cell adhesion, proliferation and differentiation.[34,38,39] Although there are a few studies that report

the processing of pure SS into a diverse set of biomaterials, including films/membranes/patches,[40] hydrogels or sponges,[41–43] in most of the studies SS has been combined with other biomaterials to form thin films,[40,43–45] membranes,[46] particles,[47,48] hydrogels,[36,43,49–52] scaffolds,[53,54] or sponges [42,43] for being used in a wide variety of biomedical scenarios owing to its hydrophilic nature and weak mechanical properties.[45,55–57]

However, in contrast to the development of Layer-by-Layer (LbL)-driven SF-based multilayered assemblies, the assembly of water-soluble SS-based supramolecular multilayered biomaterials has not yet been pursued, despite their intrinsic potential to recreate the nanofibrous structure, composition and functional complexity of the native ECM and be used in a miscellaneous range of biomedical purposes, including as implantable biomaterials.

Herein, we explore for the first time the development of cytocompatible supramolecular nanostructured multilayered thin films encompassing negatively charged SS and positively charged CHT by combining the molecular self-assembly approach with the 'greener' electrostatic-driven LbL assembly nanotechnology. Such supramolecular nanofilms aim to recapitulate the nanofibrous structure and the composition of the native cellular microenvironment, and to modulate cell functions in multiple tissue engineering strategies. CHT biopolymer was chosen as the naturally occurring cationic biopolymer owing to its proven biocompatibility, biodegradability, non-cytotoxicity, non-immunogenic properties, hydrophilicity, and close structural similarity to the glycosaminoglycans widely present in the native ECM.[58] In addition, CHT is a wide and readily available renewable polysaccharide obtained after the deacetylation of chitin, the second most abundant biopolymer in nature, which has been widely discarded as a by-product of mainly crustacean shells. As such, the potential of CHT as a sustainable and cost-effective biomaterial for biomedical applications is also underestimated.

The build-up and stability of the hybrid SS/CHT supramolecular multilayered thin nanofilms were monitored *in situ* by the quartz crystal microbalance with dissipation monitoring (QCM-D), as well as by attenuated total reflectance-Fourier transform infrared spectroscopy (ATR-FTIR). Moreover, their nanofibrillar morphology, microstructure, and wettable properties were assessed as a function of the number of layers by scanning electron microscopy (SEM), atomic force microscopy (AFM), Raman spectroscopy, and water contact angle (WCA), respectively. The *in vitro* biological performance of the SS/CHT supramolecular multilayered thin nanofilms towards human dermal fibroblasts cell line was also studied, revealing their cytocompatibility and, thus, potential to be used as sustainable implantable biomaterials for modular tissue engineering and regenerative medicine strategies.

EXPERIMENTAL SECTION

Materials

CHT with a molecular weight (M_W) of 133.76 kDa, viscosity ~71 cP, and a deacetylation (DA) degree of 96.6% was kindly provided by Primex ehf® (Siglufjordur, Iceland) and used without further purification. *Bombyx mori* cocoons were supplied by the sericulture of the Portuguese Association of Parents and Friends of Mentally Disabled Citizens (APPACDM, Castelo Branco, Portugal. Glacial acetic acid (CH_3COOH), sodium acetate trihydrate ($CH_3COONa{\cdot}3H_2O$) and hydrogen peroxide (H_2O_2) were purchased from JMGS (Odivelas, Lisboa, Portugal) and Carlo Erba (Sabadell, Barcelona, Spain), respectively. Trypsin-EDTA detaching solution and AlamarBlue were acquired from Laborspirit (Merck-Sigma, Portugal) and Invitrogen, respectively. All other reagents, namely ammonium hydroxide (NH_4OH), Dulbecco's phosphate buffered saline without Ca^{2+} and Mg^{2+} (DPBS, pH = 7.4), Dulbecco's Modified Eagle Medium/Nutrient Mixture F-12 (DMEM/F-12) basal medium, fetal bovine serum (FBS), penicillin, streptomycin and live/dead kit were purchased from ThermoFisher

Scientific (Alfagene, Carcavelos, Portugal). All the aqueous solutions were prepared using ultrapure water from a Milli-Q Plus water purification system (resistivity >18.2 MΩ.cm) from Merck Millipore (Burlington, MA, USA).

Extraction of silk sericin from *Bombyx mori* cocoons

Mulberry silkworm *Bombyx mori* cocoons were genetically controlled at the Research Centre of Agriculture and Environment (AA) – Sericulture Laboratory of Padua, University of Padua, Italy, a global leader in sericulture innovation, quality, and traceability. Cocoons' breeding and manipulation were carefully conducted under aseptic conditions, following international standards at APPACDM Sericulture in Castelo Branco, Portugal. The cocoons were cleaned, cut into fragments of ~1x1 cm^2 each, and immersed in deionized water in a proportion of 1:100 (w/v) at 100 °C for 60 min. After this period, the sericin solution was concentrated by controlled evaporation to reach 80% of evaporated water, as described in our previous work.[41] The mixture solution was filtered and then diluted to a concentration of 0.4 mg mL^{-1}, determined by the dry weight method at 105 °C for 24 h, for the build-up of the supramolecular multilayered thin films with the CHT biopolymer. The SS stock solution was kept at 4 °C until use. The M_W distribution of sericin was determined to range from 40 to 440 kDa, with the highest expression of molecular fractions being between 100 and 200 kDa, as previously described.[41]

Circular dichroism (CD) spectroscopy

The CD spectra of freshly prepared 0.04 mg mL^{-1} SS in deionized water, 0.05 mg mL^{-1} CHT in 0.1 M acetate buffer at pH 5.5, and SS/CHT (0.9:1, v/v) mixture were recorded at room temperature in a JASCO J-1500 (USA) spectrometer from 190 to 300 nm, using a high performance quartz glass cell with a path length of 2 mm (Hellma Analytics), at a scanning

speed of 100 nm min^{-1}, a digital integration time of 4 s, a bandwidth of 1 nm, a data pitch of 0.1 nm and standard sensitivity. The measurements were repeated three times and averaged for each sample.

Attenuated total reflectance-Fourier transform infrared (ATR-FTIR) spectroscopy

The ATR-FTIR spectra of the dried SS, CHT, and SS/CHT (0.9:1, v/v) thin films, as well as $(SS/CHT)_n$ supramolecular multilayered thin films (*n* referring to the number of adsorbed layers) deposited over the Au-coated glass substrates were acquired in the absorbance mode using a Bruker TENSOR 27 FTIR spectrometer (Thermo Scientific, USA) fitted with a "Golden Gate" ATR module equipped with a diamond crystal. All data were obtained in the spectral range of 4000-400 cm^{-1} by averaging 1024 individual scans per sample at a resolution of 4 cm^{-1}. All data were linear baseline corrected and normalized using the OPUS spectroscopy software supplied with the instrument.

Powder wide-angle X-ray scattering (WAXS)

Prior to the WAXS measurements, SS, CHT, and SS/CHT aqueous solutions were lyophilized for two days. Afterwards, the diffraction patterns of the individual components and co-assembled mixture in powder form were collected at room temperature on an Empyrean PANalytical diffractometer (Almelo, The Netherlands) equipped with a PIXcel1D detector (active length = 3.3473°) operating at a fixed divergence slit of 0.25°, and a spinner flat sample holder in a Bragg–Brentano *para*-focusing optics configuration. Diffraction intensity data were collected in the 2θ range between 5-60° using CuKα radiation filtered in Ni under beam conditions of 45 kV and 40 mA. Data were collected by the continuous counting method assuming a scanning step size of 0.0263° and a scanning rate of 0.02° min^{-1}. The resulting

WAXS patterns were analyzed using the HighScore Plus software and the ICDD PDF4+ (2019 release) database. The Bragg's law was used to calculate the interplanar spacing distance (*d*).

Zeta (ζ)-potential and dynamic light scattering measurements

To assess the possible interaction between SS and CHT and the build-up of $(SS/CHT)_n$ multilayered assemblies, the net electrical charge of the freshly prepared 0.4 mg mL^{-1} SS and 0.5 mg mL^{-1} CHT aqueous solutions at the working pH of 7.0 and 5.5, respectively, was investigated by measuring their zeta (ζ)-potential. The ζ-potentials of both individual solutions after filtration (25 mm syringe filters with 0.22 µm cellulose acetate membrane, VWR) were measured at 25 °C, based on the electrophoretic mobility (*u*) under an electric field, using a Zetasizer Nano-ZS (Malvern Instruments Ltd., Royston, Hertfordshire, UK). The *u* was converted into a ζ-potential value using the Smoluchowski equation ($\zeta = u\eta/\varepsilon$; η and ε refer to the viscosity and permittivity of the solution, respectively).[59] The same apparatus was used to measure the average particle size, expressed as the average hydrodynamic diameter (Z-average), and the particle size distribution, expressed as polydispersity index (PDI) of the 0.4 mg mL^{-1} SS and 0.5 mg mL^{-1} CHT aqueous solutions at pH 7.0 and 5.5, respectively, by means of dynamic light scattering (DLS) at a scattering angle of 173° (backscatter). The ζ-potential and DLS measurements were performed in triplicate and averaged for each sample.

Build-up of the supramolecular multilayered thin films by quartz crystal microbalance with dissipation monitoring (QCM-D)

The build-up of the supramolecular multilayered thin films encompassing multilayers of oppositely charged SS and CHT onto the gold (Au)-coated 5 MHz AT-cut quartz crystal sensors (AWS SNS 000043 A, Advanced Wave Sensors, Spain) was monitored *in situ* by QCM-D operating in an automatic manner (QSense Pro, Biolin Scientific, Gothenburg,

Sweden). Prior to the QCM-D experiments, the Au-coated quartz crystal sensors were submitted to UV/ozone treatment (UV/Ozone ProCleaner 220, BioForce Nanosciences, Inc.) for 10 min, followed by immersion in a 5:1:1 ultrapure water: ammonia (NH_4OH, 25%): hydrogen peroxide (H_2O_2, 30%) (v/v) oxidizing cleaning solution in an ultrasound bath at 70 °C for 10 min to remove any organic contaminants from the sensors surface. Then, the quartz crystal sensors were immediately thoroughly rinsed with ultrapure water at room temperature, dried under a soft stream of N_2, and resubmitted to UV/Ozone treatment for 10 min. Then, the freshly cleaned Au-plated quartz crystal sensors were immediately inserted in the QCM-D apparatus, equilibrated in ultrapure water until a stable baseline was achieved, and further functionalized with multilayers encompassing oppositely charged SS and CHT for assessing the possible build-up of the $(SS/CHT)_n$ multilayered thin films. Briefly, 0.4 mg mL^{-1} SS and 0.5 mg mL^{-1} CHT solutions in ultrapure water (pH 7) and 0.1 M acetate buffer (pH 5.5), respectively, were alternately pumped into the QCM-D chamber for 5 min each, thus rendering the Au-plated quartz crystal surface negatively and positively charged, respectively. In-between the deposition of both biopolymeric materials, the quartz crystal substrates were rinsed with ultrapure water (pH 7) and 0.1 M acetate buffer (pH 5.5), respectively, for 3 min each to remove loosely bounded molecules.[60] The assembly process was repeated six times until reaching $(SS/CHT)_6$ supramolecular multilayered thin films, followed by drying the LbL assemblies under a soft stream of N_2. All experiments were performed at 25 °C and at a constant flow rate of 50 µL min^{-1}.

The Au-plated quartz crystals sensors were excited at multiple overtones (1^{st}, 3^{rd}, 5^{th}, 7^{th}, 9^{th}, 11^{th}, and 13^{th} corresponding to 5, 15, 25, 35, 45, 55, and 65 MHz, respectively) and changes in the frequency (Δf) and in dissipation (ΔD) were monitored in real time. The frequency of each overtone was normalized to the fundamental resonant frequency (5 MHz) of the quartz crystal substrate ($\Delta f_n/n$; n denotes the overtone number). The results presented herein correspond to

the frequency and energy dissipation shifts associated with the 7th overtone (n = 7; 35 MHz), as they presented the lowest level of noise. Nevertheless, the results are representative of the other overtones. The hydrodynamic thickness of each adsorbed layer and final multilayer film was estimated using the Voigt-based viscoelastic model,[61] implemented in the QSense Dfind software (Broadfit function), assuming a fluid density and a layer density of 1000 kg m^{-3}, and a fluid viscosity of 1 mPa s.

The (SS/CHT)$_n$ supramolecular multilayered thin films were similarly deposited onto freshly cleaned Au-coated glass substrates (IK4-Tekniker, thickness of the Au layer: 50 nm, respectively; substrate size: 1×1 cm^2) by manual dipping for the ATR-FTIR spectroscopy, WCA, SEM, AFM, Raman spectroscopy, and *in vitro* cell culture assays. Briefly, the Au substrates were cleaned following the same procedure as reported for the QCM-D sensors. Then, the substrates were alternatively and repetitively immersed in SS (0.4 mg mL^{-1} in ultrapure water at pH 7) and CHT (0.5 mg mL^{-1} in 0.1 M acetate buffer pH 5.5) aqueous solutions for 5 min each until achieving the (SS/CHT)$_n$ multilayered thin film with the desired number of layers (n). In-between the deposition of each biopolymeric solution, rinsing steps in ultrapure water (pH 7) and 0.1 M acetate buffer (pH 5.5), respectively, were applied for 3 min each to remove weakly adsorbed molecules and avoid the cross-contamination of the biopolymeric materials' solutions.

Raman spectroscopy

The Raman spectra of the (SS/CHT)$_n$ supramolecular multilayered thin films and individual SS and CHT biopolymers deposited onto the Au-coated glass substrates were recorded on a Raman-AFM-SNOM confocal microscope WITec alpha300 RAS$^+$ (WITec, Ulm, Germany) operating in the Raman shift range of 20-3700 cm^{-1}. An Nd:YAG (neodymium-doped yttrium aluminium garnet) laser operated at 532 nm was used as the excitation source with the power

set between 4 and 5 mW. Raman spectra were collected with a 100x objective lens with an acquisition time of 2 s and 10 acquisitions. The Project 5.0^{+} program (WITec, Ulm, Germany) was used to remove the baseline of all Raman spectra (Function Shape command – Shape size: 300; Noise factor: 2). The deconvolution of the Raman spectrum of $(SS/CHT)_{15}$/SS supramolecular multilayered nanofilm in the amide I region was performed using Origin 18 software (OriginLab) and the band was fitted using the Gaussian function.

Water contact angle (WCA) measurements

The wettability of the $(SS/CHT)_n$ supramolecular multilayered nanofilms and individual SS and CHT biopolymeric materials deposited onto the Au-coated glass substrates was assessed in air through the static sessile drop method in an OCA DataPhysics 25 apparatus (Data Physics Instruments, Germany). The WCA measurements were carried out at room temperature by creating ultrapure water drops of 5 μL at the syringe's tip, followed by placing them over the functionalized Au-plated substrates. The SCA 20 software was used for the analysis of surface-drop contact angles at each surface. The measurements were repeated three times per sample at different locations on the surface and averaged for each formulation.

Atomic force microscopy (AFM)

AFM imaging on the $(SS/CHT)_n$ supramolecular multilayered thin films deposited onto the Au-coated glass substrates was performed in a combined Raman-AFM-SNOM confocal microscope WITec alpha300 RAS^{+} (WITec, Ulm, Germany) in the tapping mode (AC-AFM). A tip-cantilever silicon reflex-coated with a spring constant of 42 N m^{-1} and a typical resonance frequency of 285 kHz was used for this purpose. The images were scanned in the topography, amplitude and phase mode, and are representative of 10×10 μm^2 (1024×1024 pixel^2 with a scan speed of 2 s/line) and 5×5 μm^2 (512×512 pixel^2 with a scan speed of 1 s/line) regions over

different areas on the studied surfaces. Raw AFM data were processed by flattening and plane fitting using the Project 5.0^{+} program.

Scanning electron microscopy (SEM)

The surface morphology of the (SS/CHT)$_n$ supramolecular multilayered thin films and individual SS and CHT biopolymeric materials deposited onto the Au-coated glass substrates, as well as CHT (native), SS, and SS/CHT powders obtained after freeze-drying (CoolSafe freeze-dryer, Labogen, Denmark), was analyzed on an ultrahigh-resolution field emission gun scanning electron microscope (HR-FESEM Hitachi SU-70, Hitachi High-Technologies, Japan) operated in the secondary electrons mode at an accelerating voltage of 15 kV. Prior to the SEM analysis, the Au-coated glass substrates containing the adsorbed layers and the SS, CHT, and SS/CHT powder formulations were separately fixed to aluminum stubs by double-sided carbon conductive adhesive tape and sputtered with a conductive gold/palladium layer using a Polaron E5000 supper coater (Quorum Technologies, Laughton, UK).

Metabolic activity and viability assays

A primary human adult dermal fibroblast cell line (HDF, ATCC® PCS-201-012™) was cultured in 75 cm^2 cell culture flasks containing DMEM/F-12 medium supplemented with 10% (v/v) FBS and 1% (v/v) antibiotic-antimycotic solution in a humidified atmosphere at 37 °C and 5% CO_2. Before the *in vitro* assays, the bare Au, SS-, CHT- and (SS/CHT)$_{15}$-functionalized Au-coated glass substrates (1×1 cm^2) were exposed to UV light irradiation for 40 min to sterilize the samples. Then, the substrates were incubated, in triplicates, in 1 mL of supplemented medium in 24-well plates at 37 °C, 5% CO_2, and fully humified for 3 days. The resulting mediums with the compounds released from the substrates were used for the cell metabolic activity and viability assays, following the ISO 10993-5:2009.[62]

Upon reaching 70-80% of confluence, HDFs were detached using trypsin-EDTA and seeded in 24-well plates at a density of 20×10^3 cells per well and allowed to adhere for 24 h at 37 °C in a humified atmosphere containing 5% CO_2. Then, the culture medium was replaced by the culture medium containing the extracts released from the substrates for 3 days. After 3- and 7-days of incubation, the medium was replaced by culture medium containing 10% alamarBlue reagent. After 4 h of incubation at 37 °C and 5% CO_2, the medium of each sample was collected and transferred to a 96-well plate. The cell metabolic activity was calculated by measuring the fluorescence intensity of the medium at an excitation/emission of 540/600 nm, using a multimode microplate reader (Synergy HTX Biotek, Izasa Scientific, Carnaxide, Portugal). The experiments were performed in triplicate (n = 3) and the results were normalized to the bare Au substrate set as 100% viability.

The cell viability was assessed in a reminiscent manner via a live/dead assay. After 3 and 7 days of culture, HDF cells were stained with calcein-AM (1:500 in DPBS) and propidium iodide (1:1000 in DPBS) for 30 min at 37 °C, protected from the light. Then, the cells were washed twice with DPBS and immediately visualized by fluorescence microscopy.

Fluorescence microscopy

Fluorescence microscopy micrographs of the cells cultured with the medium containing the extracts released from the bare Au, single layer CHT- and SS-, and $(SS/CHT)_{15}$ multilayered film-functionalized Au substrates were acquired in an upright motorized widefield fluorescence microscope (Axio Imager M2, Carl Zeiss, Jena, Germany) equipped with a 200 W HXP lamp, a 3.0 Mpix monochromatic camera (Axiocam 105 mono; Carl Zeiss, Jena, Germany), and 5x and 10x objectives (Carl Zeiss, Jena, Germany). Acquired data were processed in the Zeiss ZEN v2.3 blue edition software.

Statistical analysis

Unless otherwise noted, all experiments were performed in triplicate ($n = 3$) and the results presented as mean ± standard deviation (SD). The statistical analysis was performed by one-way ANOVA followed by Tukey's post-hoc multiple comparison test using the GraphPad Prism 9.4.0 software (GraphPad Inc.). Statistically significant differences were considered for **** $p \leq 0.0001$, *** $p \leq 0.001$, ** $p \leq 0.01$, and * $p \leq 0.05$.

RESULTS AND DISCUSSION

Characterisation of the biopolymers and supramolecular co-assemblies

Figure 1a showcases the chemical structures of SS and CHT biopolymers used for the development of the SS/CHT supramolecular co-assemblies and supramolecular nanostructured multilayered thin films.

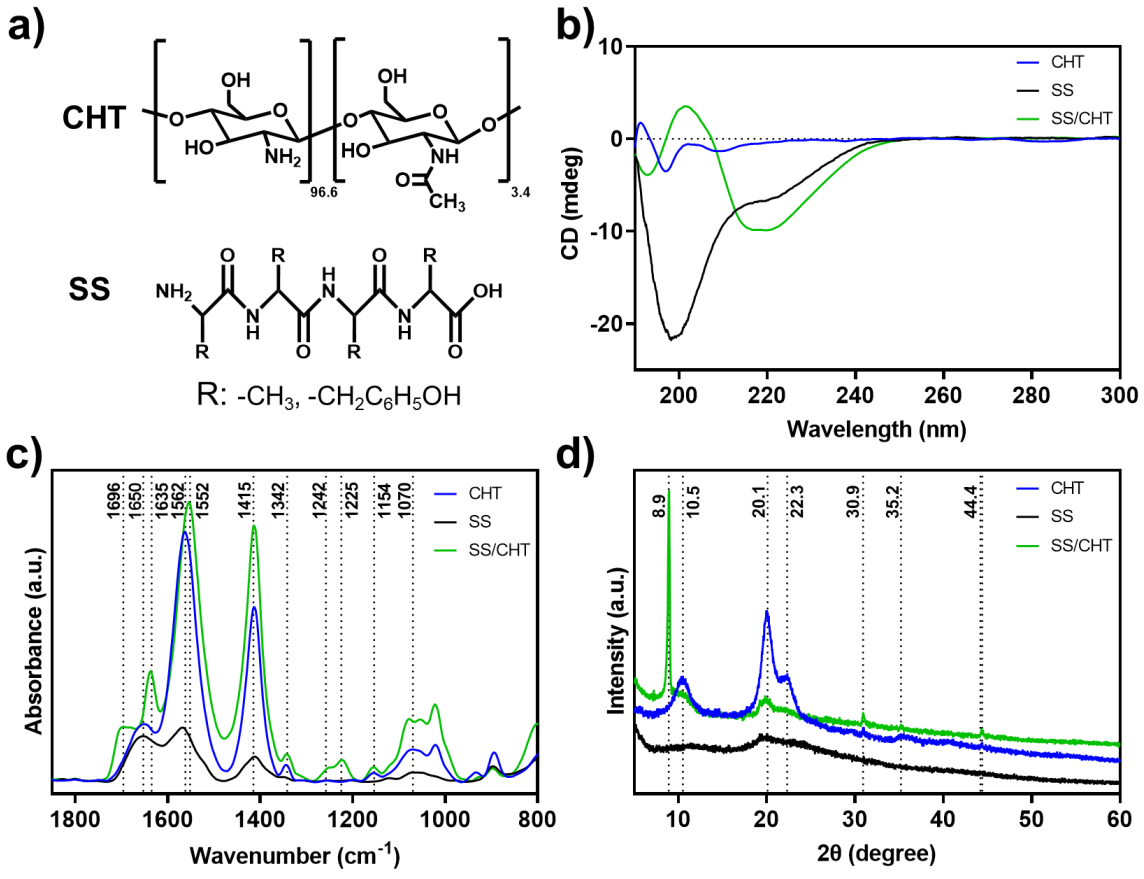

Figure 1. (a) Chemical structures of CHT and SS biopolymers. Secondary structure analysis of the individual components (SS and CHT) and co-assembled system (SS/CHT, 0.9:1 v/v) using (b) CD, (c) ATR-FTIR, and (d) WAXS.

The far-UV CD (Figure 1b) and ATR-FTIR spectroscopy (Figure 1c) were used to investigate the secondary structure and conformation of the individual SS and CHT biopolymers, as well as SS/CHT co-assembled biomaterials' solutions at room temperature. Figure 1b reveals that the SS, CHT, and SS/CHT solutions displayed, as expected, distinct spectral patterns, meaning that they adopted different conformations. The CD spectrum of SS mostly adopted a random coil configuration with a small contribution of β-sheet conformation, as illustrated by the presence of two negative minimums at ~199 and 219 nm, respectively.[63,64] The CD spectrum of CHT showed a small broad negative peak at ~209 nm, characteristic of a random coil conformation, due to the n-π* transition of the carbonyl group within the *N*-acetyl-*D*-glucosamine (-NHCO-) chromophore.[65] The co-assembly of the anionic SS with oppositely charged CHT (0.9:1 v/v) revealed the formation of a β-sheet structure with a positive maximum at ~200 nm and a negative minimum at ~219 nm. At this stage, we hypothesize that the positively charged CHT triggered the self-assembly of the oppositely charged SS via charge neutralization and led to the formation of β-sheet structures. However, to assess the potential impact of the pH change upon the co-assembly of the SS aqueous solution at pH 7 with the CHT aqueous solution at pH 5.5, CD measurements were attempted with both individual SS and CHT, and SS/CHT aqueous solutions at pH 5.5 (Figure S1). The CD spectrum of SS revealed the formation of a strong negative band at ~199 nm assigned to the random coil conformation and a weak negative band at 219 nm assigned to the β-sheet conformation. The CD spectrum of SS/CHT co-assembly (0.9:1 v/v) revealed the formation of β-sheet secondary structures, illustrated by the presence of a positive maximum at ~200 nm and a negative

minimum at ~220 nm. The CD data suggest that the co-existence of CHT in SS triggered the conformational change of SS from random coil configuration to *β*-sheet conformation, thus supporting our hypothesis that the electrostatic interactions between the SS and CHT biopolymers seem to be the main driving force enabling *β*-sheet secondary structure formation. However, it is worth noting that other intermolecular interactions (e.g., hydrophobic interactions, hydrogen bonding) may also contribute to the assembly process, although to a less extent.

Complementary to the CD analysis, ATR-FTIR measurements were also performed on dried films of native SS and CHT, and on the SS/CHT co-assembled system (0.9:1 v/v) to assign the structural features and characteristic vibration peaks of each component at the molecular level, as well as the ones corresponding to the mixture (Figure 1c). The ATR-FTIR spectrum of SS displayed prominent peaks at 1650, 1562 and 1242 cm^{-1} assigned to the amide I, II and III, respectively.[66] The peak at 1650 cm^{-1} (amide I), also denoted on the spectra of CHT, is ascribed to a random coil structure,[67] and mainly represents the C=O stretching vibration of the amide group (-NH-C=O).[56] The sharp peak in the amide II region (~1562 cm^{-1}), also observed on the spectra of CHT and SS/CHT co-assemblies, is assigned to the N-H in-plane bending and C-N bending vibrations.[68] The amide III vibrational weak peak (1200-1290 cm^{-1}), also observed in the spectra of both CHT and SS/CHT mixture, is mainly assigned to the C-N stretching vibration coupled with N-H in-plane bending.[56,68,69] The absorption bands at 1342, 1415, 1154 and 1070 cm^{-1}, which were also observed on the spectra of both CHT and SS/CHT co-assemblies, are attributed to the C-N stretching vibration, -CH coupled with O-H in-plane bending vibration, and asymmetric C-O-C stretching and C-O stretching vibrations of the saccharide rings, respectively.[68,70,71]

The ATR-FTIR spectrum of the SS/CHT mixture revealed a sharp peak at ~1635 cm^{-1} (amide I), indicative of the presence of a strong intramolecular *β*-sheet conformation.[72,73] Moreover,

the appearance of a peak at 1696 cm^{-1} (amide I) indicates the formation of a hydrogen bonding β-sheet intermolecular structure with preferentially an antiparallel orientation.[67,70,72]

To obtain further structural information on the molecular arrangement and identify the crystalline and/or amorphous nature of the samples, the microstructural analysis of the SS, CHT, and SS/CHT co-assembled system was performed by WAXS (Figure 1d). The WAXS diffraction pattern of SS revealed a weaker and broader diffraction peak with a maximum at 2θ = 20.1°, which indicates the predominant amorphous and disordered nature of SS and, thus, its higher content of random coil conformation.[74] The diffraction pattern of native CHT showcased two main characteristic peaks at 2θ = 10.5° and 20.1°, which are assigned to the semi-crystalline structure of CHT which is stabilized by intra- and intermolecular hydrogen bonding established between the hydroxyl and amino functional groups present in the polymeric chain.[75,76] The diffraction pattern of the SS/CHT co-assembly denoted considerable differences when compared with the SS and CHT patterns, as well as the appearance of new diffraction peaks, such as a very sharp and highly intense diffraction peak at 2θ = 8.9°, which is indicative of a highly crystalline structure. The interplanar spacing (d) of the crystallites in the SS/CHT co-assembly at 2θ = 8.9° was determined following the Bragg's law ($d = (n\times\lambda)/2\times\sin\theta$, where d is the interplanar spacing, n is the order of reflection, λ is the wavelength, and 2θ is the peak position), reaching to a value of *ca.* 10 Å. This is a typical distance of an antiparallel β-sheet structure, known to be tightly packed with a higher supramolecular order.[77] This diffraction peak is assigned to the intermolecular hydrogen bonding between the hydroxyl groups of the amino acids present in the SS and the amino groups present in the CHT structures. Moreover, the full width at half-maximum (FWHM) was used to calculate the crystallinity of the SS/CHT co-assembly, leading to a crystal size of *ca.* 45 nm. All the other weak and sharp diffraction peaks at 2θ = 30.9°, 35.2°, and 44.4° suggest the predominance of crystalline phases. Moreover, the diffraction peak at 2θ = 20.1° became sharper when compared with the same peak obtained

for the native SS, thus meaning that there is an increase in the crystalline structure and, therefore, a higher degree of *β*-sheet conformation. The diffraction patterns corroborate the CD, and ATR-FTIR data, revealing the formation of a highly ordered *β*-sheet secondary structures in the SS/CHT co-assembled system.

The morphology and microstructure of the SS and SS/CHT co-assembled supramolecular system after freeze-drying, as well as of the CHT biopolymer (native, without freeze-drying) were investigated by SEM (Figure 2). The SEM micrograph of the SS (Figure 2a) revealed the presence of sheet-like structures along with fibrils linked to spheres in a beaded form, which are characteristic of SS, and the micrograph of the CHT (Figure 2b) showcased the presence of larger flakes in bulk. The micrograph of the SS/CHT co-assembly clearly revealed the formation of an entangled network of fibers with 3D interconnectivity, which formed a highly porous network structure (Figure 2c). The diameters of the individual fibrils ranged from 200-700 nm, and up to 9 μm when an intensive aggregation and association of SS molecules triggered by CHT biopolymer was denoted. Therefore, the SEM imaging results corroborate the CD, ATR-FTIR, and WAXS data, as supramolecular fiber network structures are typically formed by *β*-sheet structures.

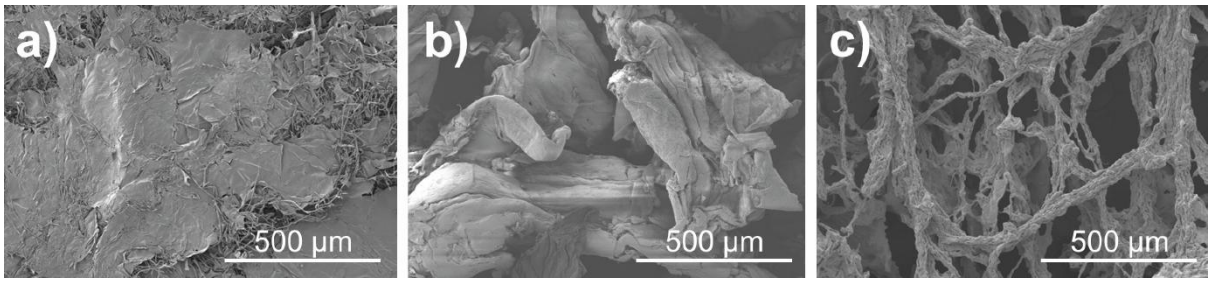

Figure 2. Representative SEM micrographs of (a) SS, (b) CHT, and (c) SS/CHT (0.9:1 v/v) co-assembled system obtained in the secondary electrons mode. The magnification factor is 100× in all images.

Build-up of SS/CHT supramolecular multilayered thin films

Prior to the build-up of the SS/CHT supramolecular multilayered thin nanofilms, the net electrical charges of the freshly prepared 0.4 mg mL^{-1} SS and 0.5 mg mL^{-1} CHT aqueous solutions at pH 7 and 5.5, respectively, were assessed by measuring their ζ-potentials. The ζ-potential measurements of SS and CHT solutions were found to be –21.4 ± 1.5 and +24.7 ± 1.2 mV, respectively, thus revealing their anionic and cationic nature and, thus, the possible build-up of electrostatically-driven SS/CHT supramolecular multilayered thin films.

The QCM-D technique was used to monitor the build-up of the $(SS/CHT)_6$ supramolecular multilayered thin films by applying an alternating electric field across the Au-coated quartz crystal sensor.[78]

Figure 3a showcases the $\Delta f_n/n$ and ΔD_n obtained at the 7th overtone (n = 7; 35 MHz) for the build-up of $(SS/CHT)_6$ supramolecular multilayered thin films onto the Au-plated quartz crystal substrates. The sequential decrease in the $\Delta f_7/7$ over time after the adsorption of each of the SS and CHT layers onto the Au-plated quartz crystal surface reveals the deposition of both biopolymeric materials and, thus, increase in the hydrodynamic mass per layer, as well as the effective interaction between the oppositely charged materials and the successful and stable LbL growth of the SS/CHT supramolecular multilayered thin film. Furthermore, one can denote an exponential increase in the $\Delta f_7/7$ (in moduli) over time after the adsorption of the first three SS/CHT bilayers, which implies an increase in the hydrodynamic mass per adsorbed layer.

In addition, the increase in the ΔD_7 reveals the soft and viscoelastic nature of the multilayered film, which is a typical feature of soft and hydrated polymeric systems.[21,22,70] Notably, such an increase in the ΔD_7 is much more pronounced after the assembly of the first three SS/CHT bilayers, revealing an exponential-like growth regime, which suggests that the viscoelastic properties of the multilayered film are not constant throughout the build-up process. Overall,

the gradual decrease of the frequency shift together with the increase in the energy dissipation indicates that the positively charged CHT (pH<p*K*a~6-6.5)[79] adsorbed onto the negatively charged SS layer (pH>p*I*~3.9-4.1).[80] Moreover, while the rinsing steps after the adsorption of each of the CHT layers led to negligible changes in the $\Delta f_7/7$ and ΔD_7, which indicates the strong association of the CHT layers and the irreversible nature of the adsorption process, a different behavior was observed following the adsorption of the SS layers. As for the latter, a continuous decrease in the $\Delta f_7/7$ (in moduli) and ΔD_7 was denoted following the rinsing steps, mainly after the deposition of the third SS layer. We hypothesize that this behavior might be due to the desorption of loosely bound SS molecules and SS/CHT complexes, and/or to deswelling, thus contributing to an increase in the film stiffness. To assess the potential impact of pH changes on the LbL film growth, we have built a multilayer film encompassing six bilayers of oppositely charged SS and CHT, with both biopolymeric materials being deposited in 0.1 M acetate buffer at pH 5.5. As shown in the Figure S2, the sequential decrease in the $\Delta f_7/7$ and the increase in the ΔD_7 after the adsorption of both the SS and CHT layers at pH 5.5 prove the multilayered film growth via electrostatic interactions between the negatively charged SS (ζ-potential = –14.4 ± 1.0 mV) and oppositely charged CHT (+24.7 ± 1.2 mV). The direct comparison of the build-up of the $(SS/CHT)_6$ supramolecular multilayered film assembled with SS at pH 7 and CHT at pH 5.5 (Figure 3a) with the same multilayered film assembled with both SS and CHT at pH 5.5 (Figure S2) reveals differences in the extent of the frequency shift and dissipation changes. While the multilayered film assembled at two different pH led to a $\Delta f_7/7$ of *ca.* –900 Hz and a ΔD_7 of *ca.* 200×10^{-6}, the multilayer film prepared with both biopolymers at pH 5.5 conducted to a $\Delta f_7/7$ of *ca.* –400 Hz and a ΔD_7 of *ca.* 40×10^{-6}. We hypothesize that such behavior could be related to the higher net electrical charge denoted by the SS aqueous solution at pH 7 (ζ-potential = –21.4 ± 1.5 mV) and stronger attractive electrostatic interactions with CHT (ζ-potential = +24.7 ± 1.2 mV) when compared to the SS

assembled with CHT at pH 5.5 (ζ-potential = –14.4 ± 1.0 mV), thus enabling a larger adsorbed mass of SS. In fact, the lower net electrical charged denoted by SS at pH 5.5, due to the vicinity of the protein's p*I* (~3.9-4.1), is an indication that certain parts of the protein surface may have a higher number of functional groups (more protonated amino groups) whose charge differs from the net electrical charge of the whole protein, leading to stronger repulsive electrostatic interactions between SS and CHT (stronger protein-protein interactions) and to a reduction in the number of adsorbed molecules. Moreover, larger conformational changes in the SS's secondary structure may occur upon deposition of CHT at pH 5.5 onto the SS layer (assembled at pH 7). In fact, it has been reported that larger amounts of protein and larger structural changes are found when the protein/polysaccharide charges are opposing and at stoichiometry.[81] Although one cannot neglect the influence, to some extent, of the pH changes in the build-up of the SS/CHT multilayered films, this result reveals that the electrostatic interaction between the biopolymers is the main driving force enabling multilayered film growth. However, the influence of other intermolecular interactions in the assembly process, namely hydrophobic interactions and hydrogen bonding cannot be excluded.

The QCM-D data was also used to estimate the cumulative hydrodynamic thickness of the $(SS/CHT)_6$ supramolecular multilayered films at each adsorption step using the Voigt-based viscoelastic model (Figure 3b),[61] which revealed an exponential growth regime with a maximum thickness of *ca.* 300 nm, similarly to what has been reported previously for the growth of soft biopolymeric multilayered films.[21,82] The Voigt-based viscoelastic model was applied due to the soft, hydrated, and viscoelastic nature of the biopolymeric multilayer film, which was revealed by the fact that the frequency and dissipation changes recorded for multiple overtones, i.e. $\Delta f_n/n$ and ΔD_n (n = 3, 5, 7, 9, 11), respectively, did not overlap each other and the dissipation changes were much larger than zero (see Figure S3). In this scenario, both the

adsorbed biopolymers and coupled solvent, as well as viscous effects contribute to the frequency and dissipation changes.[83]

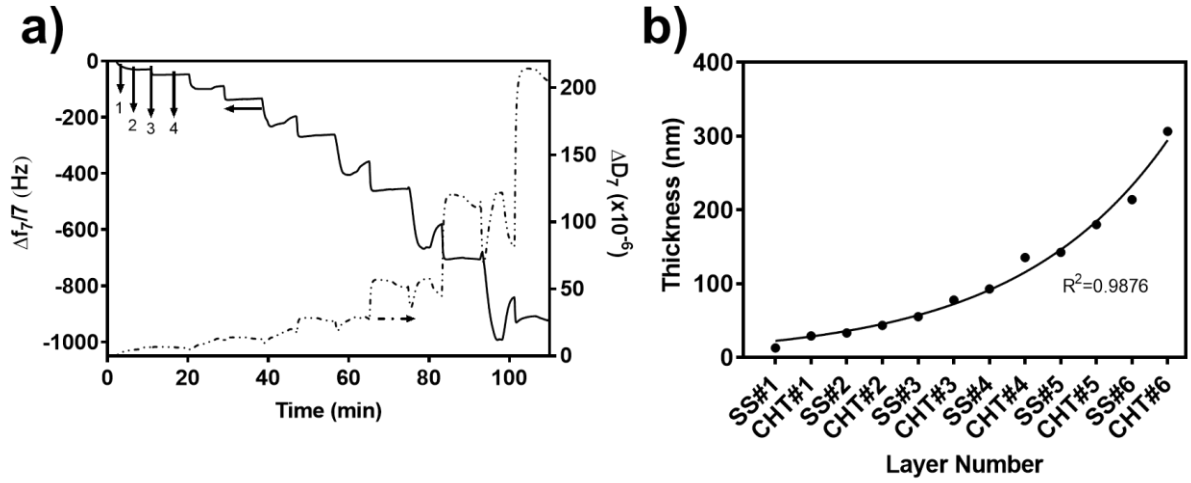

Figure 3. (a) QCM-D monitoring of the normalized frequency ($\Delta f_n/n$, straight line) and dissipation (ΔD_n, dashed line) shifts, obtained at the seventh overtone (n = 7; 35 MHz), as a function of time, for the build-up of $(SS/CHT)_6$ supramolecular multilayered thin film onto Au-coated quartz crystal sensors and intermediate rinsing steps. The inset numbers refer to the adsorption of SS (1), CHT (3), and rinsing steps (2 and 4). (b) Cumulative hydrodynamic thickness evolution for the $(SS/CHT)_6$ supramolecular multilayered thin film as a function of the number of adsorbed layers, estimated using the Voigt-based viscoelastic model. The black line represents the exponential trend line.

Physicochemical characterization of the SS/CHT supramolecular multilayered thin films

ATR-FTIR spectroscopy was also employed to monitor the build-up of SS/CHT supramolecular multilayered thin films adsorbed onto Au-coated glass substrates. Figure 4 shows the obtained spectra at different steps of the build-up of $(SS/CHT)_{15}$ multilayered thin films, revealing that the intensity of the absorbance peaks increased with the increase in the number of SS/CHT bilayers, thus proving the multilayered film growth. In particular, the increase in the absorbance was clearly denoted in the amide I (~1663 cm^{-1}), amide II (~1570

cm^{-1}), and amide III regions (~1250 cm^{-1}), which are characteristic absorption peaks of β-sheet secondary structures. Moreover, a similar behavior was observed for the absorption bands at 1422 cm^{-1}, assigned to the C-H and O-H in-plane bending vibration, at 1345 cm^{-1}, attributed to the C-N stretching vibration, and in the region 1000-1150 cm^{-1}, assigned to the asymmetric C-O-C stretching and C-O stretching skeletal vibrations of the saccharide rings.

In order to assess the potential role of the outer layer on the absorption peaks, similar multilayered thin films were assembled onto Au-coated glass substrates and further functionalized with an outer SS layer, *i.e.* $(SS/CHT)_n/SS$. Similar absorption peaks to those observed as per the $(SS/CHT)_n$ multilayered films were denoted with a slight blue shift in the characteristic absorption bands of the amide I, II and III. Interestingly, the CHT-ending multilayered films showed a higher intensity peak for amide II compared to amide I, whereas the SS-ending multilayered films displayed the opposite trend. Such behavior reveals the high amount of amine and amide functional groups in the outer region of the CHT-ended films upon adsorption of each CHT layer, and the high amount of carbonyl groups in the multilayered films having SS as the outermost layer upon adsorption of each SS layer.

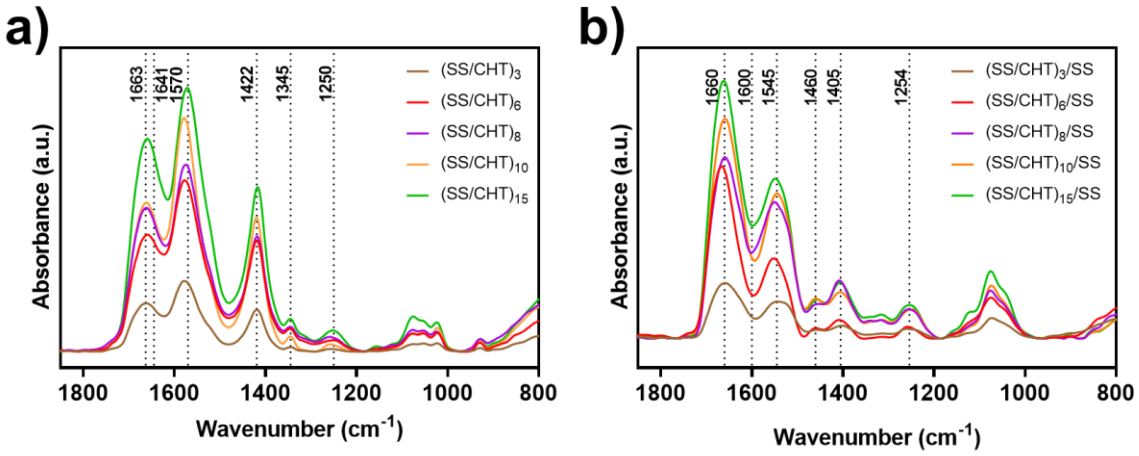

Figure 4. ATR-FTIR spectra of (a) CHT- and (b) SS-ending multilayered nanofilms with up to fifteen SS/CHT bilayers deposited over the Au-coated glass substrates. The spectra obtained

for the adsorption of either SS or CHT over the Au-coated glass substrates are also shown for comparison.

The SS-, CHT-, and $(SS/CHT)_{15}/SS$ multilayered film functionalized Au-coated glass substrates were further inspected by Raman spectroscopy to elucidate the microstructure of the assembled systems (Figure 5). The absorption bands at 1675 cm^{-1} (amide I) and ~1241 cm^{-1} (amide III) in the spectra of the $(SS/CHT)_{15}/SS$ supramolecular multilayered nanofilm indicate the presence of β-sheet conformation (Figure 5a).[84,85] The deconvolution of the amide I band (range between 1600-1710 cm^{-1}) shows that this band is composed of four components located near 1640 (5%; random coil structure), 1655 (7%; α-helix mainly due to poly-glycine), 1675 (78%; β-sheet), and 1695 cm^{-1} (10%; β-turn due to peptide bonds in type I),[86] with the 1675 cm^{-1} being by far the broader and more intense band – Figure 5b. This result demonstrates that the $(SS/CHT)_{15}/SS$ supramolecular multilayered nanofilm is composed essentially of β-sheet secondary structures, which agrees with the CD, ATR-FTIR and WAXS analysis. It should be noted that the number of components, the exact band position and the band intensity are all dependent on the type of silk.

The peak at 1460 cm^{-1}, present in all spectra, is assigned to the $-CH_2$ deformation. In the SS spectrum, the 1647 cm^{-1} peak (amide I) indicates an amorphous state (random coil conformation), whereas in the CHT spectrum this band is related to the C=O stretching vibration of the amide group.[84,87] In the amide B region, the peaks at 2844, 2888, and 2935 cm^{-1} arise from the symmetric and asymmetric $-CH_2$ stretching vibrations and symmetric $-CH_3$ stretching vibration in alkyl groups, respectively, while the peak at 2970 cm^{-1} is associated with the asymmetric -CH stretching vibration of the alkyl group. We hypothesize that the broad peak observed in the multilayered film at 3289 cm^{-1} (amide A) could be assigned to the overlapping N-H and O-H stretching vibrations, indicating intermolecular hydrogen bonding between the

hydroxyl groups of the amino acids present in the SS and the amino groups presented in the CHT.

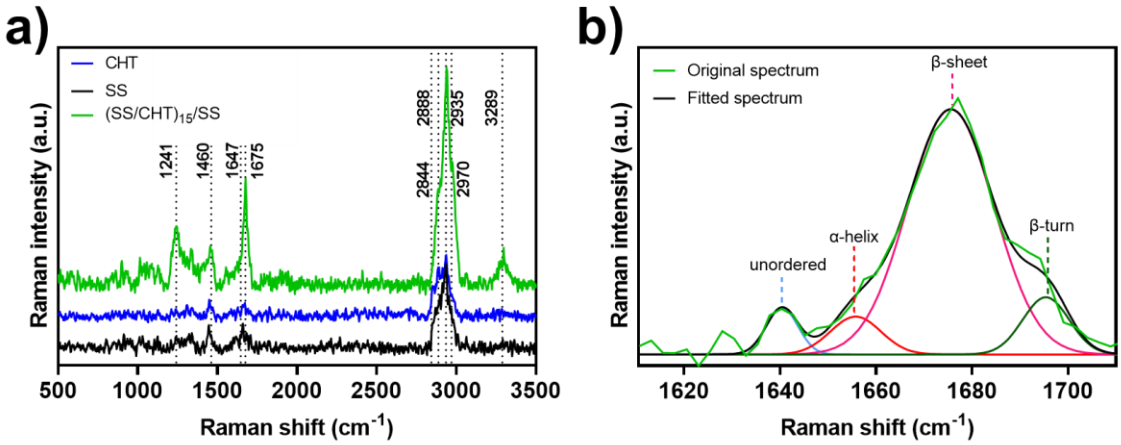

Figure 5. (a) Raman spectra of single layer SS- and CHT-, and $(SS/CHT)_{15}/SS$ multilayered thin film-functionalized Au-coated glass substrates. (b) Deconvolution of the Raman spectrum of the $(SS/CHT)_{15}/SS$ supramolecular multilayered thin film in the amide I region.

The Au-coated glass substrates functionalized with individual SS and CHT layers, as well as with $(SS/CHT)_n$ supramolecular multilayered films having either CHT or SS as outermost layers were further inspected for their wettability through WCA measurements (Figure 6). Although both CHT and SS-ending multilayered films exhibited a more hydrophilic behavior when compared to the bare Au substrate, those ending in CHT revealed a slightly more wettable state. In addition, the three bilayered films denoted the lowest WCA among the studied multilayered films, thus revealing their slightly more hydrophilic nature.

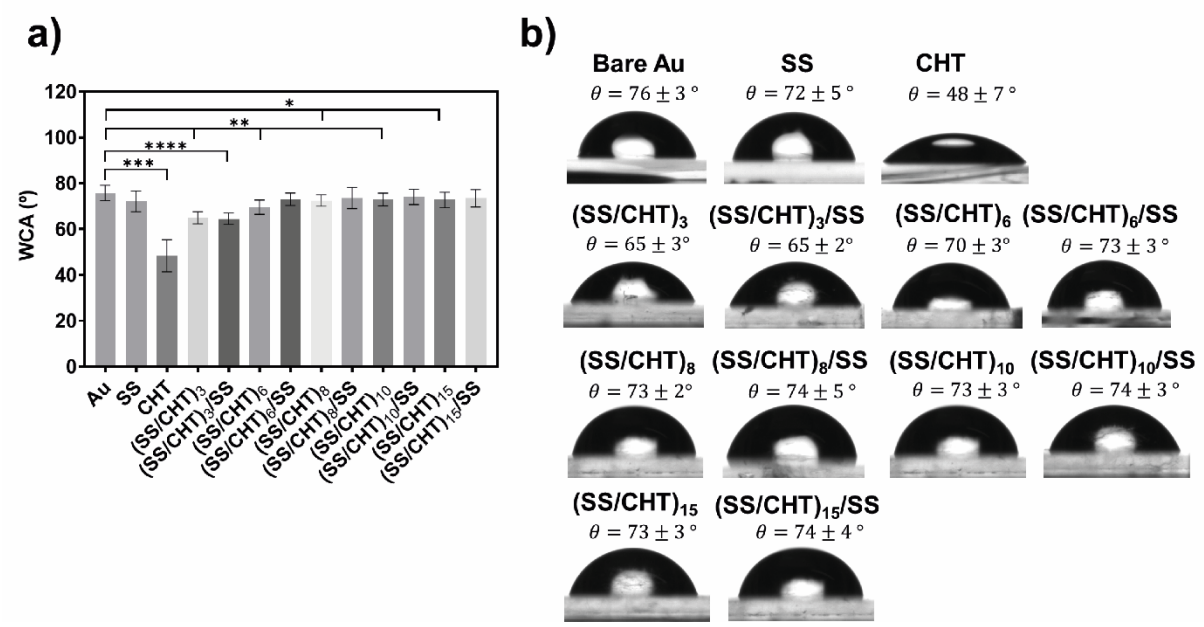

Figure 6. (a) WCA of the bare and SS-, CHT-, $(SS/CHT)_n$- and $(SS/CHT)_n$/SS-functionalized Au-coated glass substrates in ultrapure water. Data are presented as mean ± standard deviation (SD) of three independent experiments (n = 3, per condition) performed in triplicates. Significant differences were found for **** $p \leq 0.0001$, *** $p \leq 0.001$, ** $p \leq 0.01$, and * $p \leq 0.05$. (b) Representative images of ultrapure water droplets on bare and functionalized Au substrates.

Morphological analysis of the SS/CHT supramolecular multilayered thin films

The morphological and structural features of the bare Au, SS- and CHT-functionalized Au substrate, and SS/CHT nanostructured supramolecular multilayered thin films functionalized Au substrate were analyzed by SEM (Figure 7) and AFM (Figure 8). The SEM micrographs of the supramolecular multilayered films having fifteen bilayers denoted denser fibrillar-like patterns, resulting from the progressive self-assembly and bundling of SS triggered by interactions with oppositely charged CHT biopolymer (Figure 7f and g). Similar patterns were reported previously for the self-assembly of SS.[88] In contrast, the six-bilayered films showed thinner, longer, and individual fibrils in both CHT and SS-ending films (Figure 7d and e), being

more pronounced in the SS-ending multilayered films. Furthermore, the SEM micrograph of the SS-functionalized Au substrate (Figure 7b) did not show fibrillar-like structures, indicating that SS *per se* does not induce fibril formation, and thus, CHT is needed to trigger SS's self-assembling capability. In addition, the SEM micrographs of the SS- (Figure 7b) and CHT-functionalized Au substrate (Figure 7c) revealed the formation of spherical particles, which may indicate potential particle formation in the aqueous solutions of the individual biopolymers. The DLS measurements performed for the SS and CHT aqueous solutions revealed the formation of particles denoting an average hydrodynamic diameter (Z-average) of 200.8 ± 3.4 nm and 96.9 ± 7.0 nm and a bimodal distribution with a polydispersity index (PDI) of 0.9 ± 0.02 and 0.7 ± 0.02, respectively (Figure S4). Such high PDI values reveal the polydisperse nature of the particles. Moreover, the fact that the absolute ζ-potential of the aqueous solutions of both biopolymers is between 10 and 30 mV, indicates incipient instability of the colloidal particles and a tendency to flocculate.[89,90] The close look into the SEM micrographs revealed the formation of larger particles when compared to the average hydrodynamic particle size obtained by DLS measurements. We hypothesize that such larger particle aggregates could be ascribed to sample drying for enabling SEM analysis and to the lack of electrostatic repulsion between the particles.

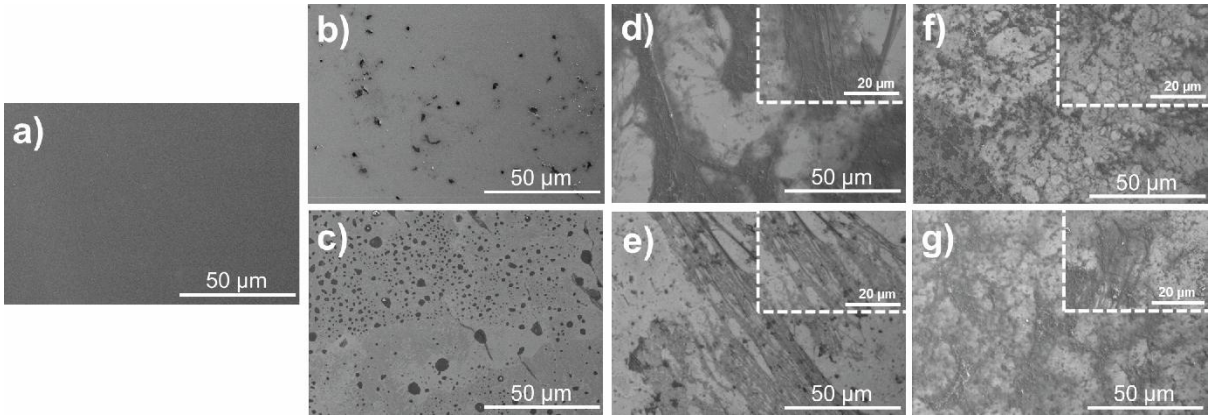

Figure 7. Representative SEM micrographs taken in high vacuum (4 kV) and secondary electrons mode over different regions of the (a) bare Au and Au-coated glass substrate

functionalized with (b) SS, (c) CHT, (d) $(SS/CHT)_6$, (e) $(SS/CHT)_6/SS$, (f) $(SS/CHT)_{15}$, and (g) $(SS/CHT)_{15}/SS$ supramolecular multilayered films. The magnification factor is 1000× (main images) and 2000× (insets).

The CHT- and SS-ending supramolecular multilayered films were also examined by AFM in tapping mode (Figure 8). The 3D AFM topographic images revealed clear morphological and structural differences between the bare and functionalized Au substrates, showcasing a transition from a smooth surface topography in the case of the bare Au substrate (Figure 8a) to a rougher surface after the deposition of both CHT- (Figure 8b,d,f) and SS-ending multilayered films (Figure 8c,e,g). This behavior was corroborated by the successive increase in the root-mean-square surface roughness (R_q) values obtained for both CHT- and SS-ending films with the increase in the number of bilayers (Figure 8h,i). However, a comparison of both multilayered thin films revealed differences in the R_q values and surface topography. The SS-ending multilayered films exhibited smaller R_q values when compared to the CHT-ending films, indicating that the SS films were smoother than the CHT-ending ones. Significant differences were observed between the SS- and CHT-ended multilayered films having fifteen bilayers (Figure 8h; main images) and between the SS- and CHT-ended multilayered films having eight and fifteen bilayers (Figure 8i; inset images). Moreover, the SS-ending films denoted the formation of a fibrillar-like pattern, which became more pronounced while increasing the number of layers, holding great promise as an ECM-mimetic fibrillar environment.

On the other hand, the CHT-ending multilayered films showed the formation of larger randomized islets across the surface. These findings were further supported by the height profiles extracted from the CHT- and SS-ending multilayered films (data not shown). The height profiles of the later revealed an increase in the height of the fibers covering the Au

surface from 17 to 60 nm upon increasing the number of bilayers in the case of the SS-ending films, while the fiber width remained *ca.* 750 nm. On the other hand, the height profiles of the CHT-ending multilayered films revealed an increase in the height of the islets deposited onto the Au surface, from 60 to 200 nm, upon increasing the number of layers, with islets' width ranging from 0.75 to 1.75 μm.

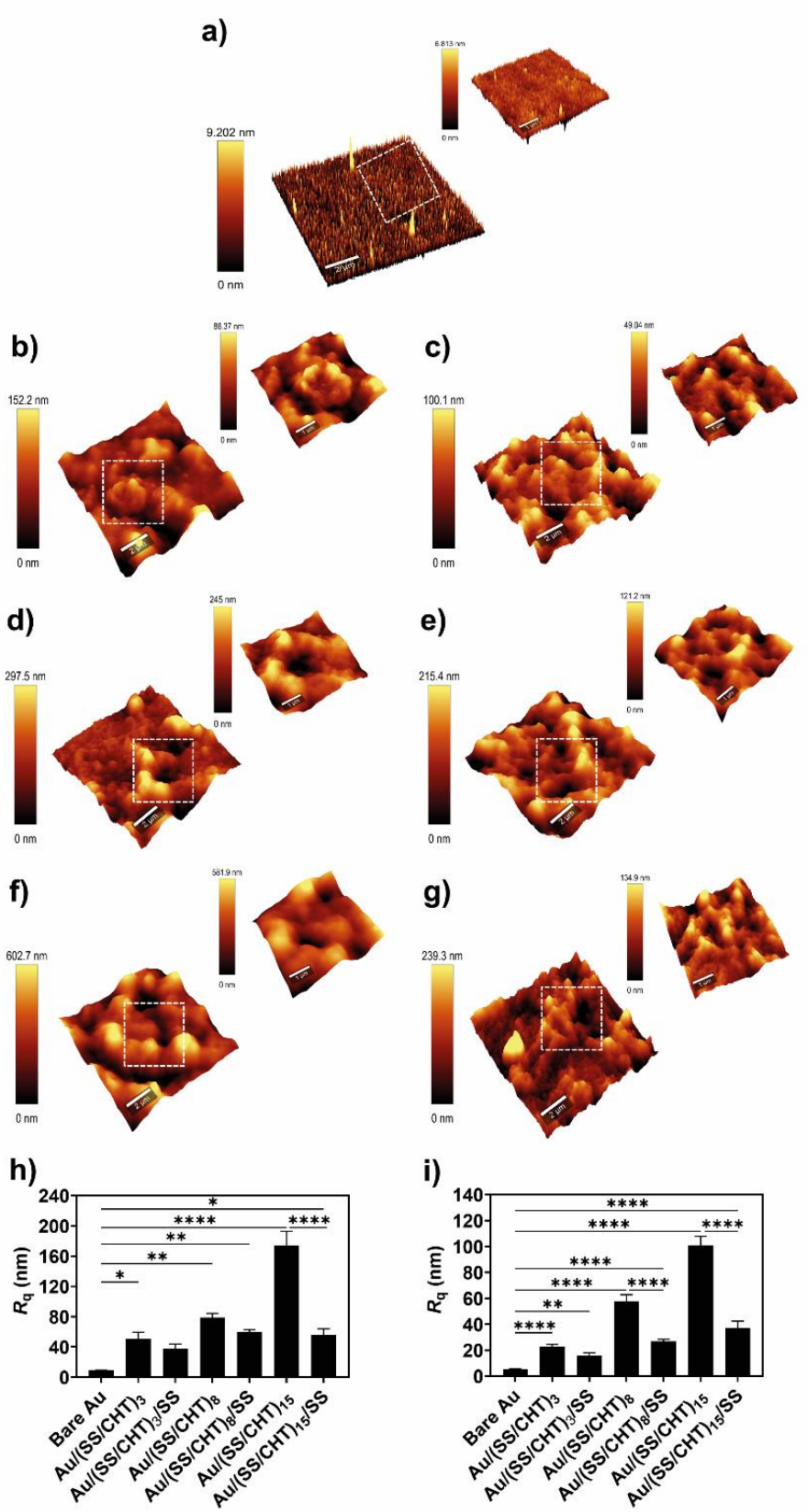

Figure 8. Representative 3D AFM topographic images taken in air for the (a) bare Au, and (b) $(SS/CHT)_3$, (c) $(SS/CHT)_3/SS$, (d) $(SS/CHT)_8$, (e) $(SS/CHT)_8/SS$, (f) $(SS/CHT)_{15}$, and (g)

$(SS/CHT)_{15}$/SS functionalized Au substrates with the respective R_q values for all surfaces. The images scan sizes are 10 × 10 μm^2 (main images) and 5 × 5 μm^2 (insets). (h, i) Root-mean-square surface roughness (R_q) obtained for all surface formulations for the images scan sizes of (h) 10×10 μm^2 and (i) 5×5 μm^2. The R_q data are presented as mean ± standard deviation (SD) of two (10×10 μm^2) and five independent areas per sample (5×5 μm^2). Significant differences were found for **** $p \leq 0.0001$, *** $p \leq 0.001$, ** $p \leq 0.01$, and * $p \leq 0.05$.

***In vitro* biological performance of the SS/CHT supramolecular multilayered thin films**

The cytocompatibility of the as-developed supramolecular multilayered thin films encompassing fifteen bilayers was assessed *in vitro* with primary human dermal fibroblasts (HDF) model cell line aiming to assess their potential to be used in biomedical applications. The cellular viability and metabolic activity were assessed on the bare Au substrate, on the single layer SS- and CHT-functionalized Au substrate, and on the $(SS/CHT)_{15}$ multilayered nanofilms functionalized Au substrate at two different time points (3 and 7 days) through a live/dead and an alamarBlue assay, respectively. The live/dead images showed that the HDF cells cultured with the culture medium containing the extracts released from the substrates remained alive and proliferated after 3 and 7 days of culture, with negligible death (Figure 9a), exhibiting an excellent cellular viability. Therefore, the live/dead assay revealed the cytocompatibility of all formulations for this cell line. Furthermore, the alamarBlue results, obtained after 3 and 7 days of culture, corroborated the high metabolic activity of HDF cells, which was similar for all surface formulations (*ca.* 100%) and within the range of the control (bare Au substrate) – Figure 9b.

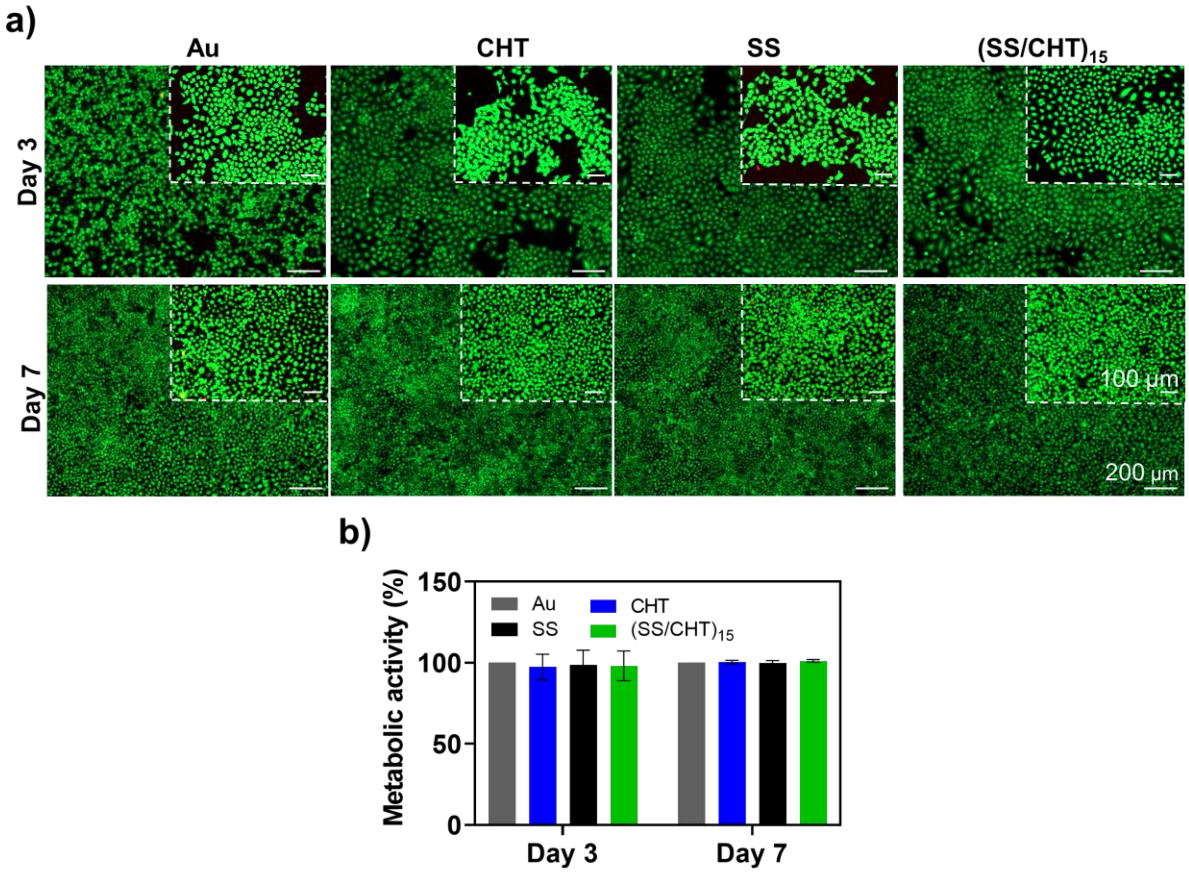

Figure 9. (a) Representative fluorescence microscopy images of live (green) and dead (red) HDF cells and (b) metabolic activity of HDFs at 3 and 7 days of *in vitro* culture with the medium containing the extracts released from the bare Au substrate, and CHT-, SS- and $(SS/CHT)_{15}$ functionalized Au substrates. Scale bars: 200 µm (main images) and 100 µm (inset images). Data presented as mean ± SD of three independent experiments (n = 3, per condition) performed in triplicates.

CONCLUSIONS

In this work, novel electrostatic-driven SS/CHT supramolecular multilayered nanofilms were successfully designed and developed by sequential deposition of SS and CHT on Au-coated surfaces. The soft multilayered nanocoatings were in-depth characterized for their physicochemical properties and cytocompatibility aiming for being used as 2D sustainable

biomaterial nanoplatforms for biomedical applications. It was shown that the CHT biopolymer triggered the self-assembly capability of SS. Moreover, the combination of the self-assembly approach with the LbL assembly technology enabled the build-up of sustainable supramolecular multilayered nanofilms denoting a fibrillar-like topography. Such supramolecular biomaterial nanocoatings demonstrated to be cytocompatible for HDF cells, as unveiled by the live/dead and alamarBlue assays. The SS/CHT supramolecular multilayered nanocoatings may be attractive fibrillar-like supramolecular matrices for cell culture.

We envisage that this work could open new avenues in the development of complex, robust, and size- and shape-tunable dynamic SS-based sustainable 2D and 3D supramolecular biomaterial platforms and biomedical devices for being used in a plethora of biomedical applications, including in controlled drug/protein/cell delivery, biosensing, and modular tissue engineering and regenerative medicine strategies. Those include free-standing multilayered membranes and hollow tubular structures denoting tunable mechanical properties that could be potentially used as smart implantable biomaterials or even as stimuli-responsive nanocarriers to be used as injectable systems for the targeted delivery of protein/therapeutics or cells. In addition, taking advantage of the high versatility and mild processing conditions imparted by the LbL assembly technology, those supramolecular multilayered nanobiomaterials may incorporate multiple ingredients, including bioactive peptide sequences, thus enabling multicomponent platforms that could more closely recreate the ECM of native tissues and be used in 3D *in vitro* modeling and regenerative medicine.

SUPPORTING INFORMATION

The Supporting Information is available free of charge at https://pubs.acs.org/doi/10.1021/acs.biomac.XXXXXXX.

- CD spectra of the aqueous solutions of the individual components (SS and CHT) and SS/CHT co-assembled system at pH 5.5; QCM-D data for the build-up of the $(SS/CHT)_6$ supramolecular multilayered thin film at pH 5.5; QCM-D data showing multiple overtones for the build-up of the $(SS/CHT)_6$ supramolecular multilayered thin film with SS assembled at pH 7 and CHT assembled at pH 5.5; DLS data showing the hydrodynamic particle size distribution of SS and CHT aqueous solutions at pH 7 and 5.5, respectively.

AUTHOR INFORMATION

Corresponding Authors

Ana L. Oliveira – CBQF-Centro de Biotecnologia e Química Fina – Laboratório Associado, Universidade Católica Portuguesa, Escola Superior de Biotecnologia, Rua Diogo Botelho 1327, 4169-005 Porto, Portugal; https://orcid.org/0000-0001-8012-4203; E-mail: aloliveira@ucp.pt (A.L.O.)

João Borges – CICECO – Aveiro Institute of Materials, Department of Chemistry, University of Aveiro, Campus Universitário de Santiago, 3810-193 Aveiro, Portugal; https://orcid.org/0000-0003-0126-8482; E-mail: joaoborges@ua.pt (J.B.)

Author Contributions

J.B. conceived and designed the project and research direction, supervised the project, provided resources and acquired funding. A.L.O. supervised the project, provided resources and acquired funding. J.F.M. provided resources and acquired funding. M.R. performed the CD, WAXS, ATR-FTIR, QCM-D and WCA experiments. C.F.V.S. and A.P. performed some of the CD and QCM-D experiments. C.F.V.S., A.P., A.J.R.A. and T.P. performed the *in vitro* cellular viability and metabolic activity assays, and fluorescence microscopy imaging. S.G.P.

acquired SEM imaging. S.F. acquired AFM imaging and some of the Raman spectra and performed the deconvolution of the Raman spectra. H.I.S.N. acquired some of the Raman spectra. C.F.V.S., A.P. and J.B. wrote the manuscript. All authors analyzed the data, discussed the results, and reviewed and edited the manuscript. All authors have given approval to the final version of the manuscript.

Notes

The authors declare no competing financial interest.

Data availability

Data supporting this work will be available from DUnAs (institutional research data repository of the University of Aveiro) at https://doi.org/10.48527/5IWKGP following a 2-year embargo period due to potential IPR issues.

ACKNOWLEDGMENTS

This work was funded by the European Union's Horizon Europe research and innovation programme under the Grant Agreement No. 101079482 ("SUPRALIFE"). This work was also funded by the Programa Operacional Regional do Centro – Centro 2020, in the component FEDER, and by national funds (OE) through Fundação para a Ciência e a Tecnologia/Ministério da Ciência, Tecnologia e Ensino Superior (FCT/MCTES), in the scope of the project "SUPRASORT" (PTDC/QUI-OUT/30658/2017, CENTRO-01-0145-FEDER-030658), as well as by the project UIDB/50016/2020 of the Centre for Biotechnology and Fine Chemistry - CBQF and "Interreg VI A España – Portugal (POCTEP) 2021-2027", IBEROS+ (0072_IBEROS_MAIS_1_E) - Instituto de Biofabricación en Red para El Envejecimiento Saludable. C.F.V.S., S.G.P. and J.B. gratefully acknowledge FCT for the individual PhD grant (2020.04408.BD, DOI 1054499/2020.04408.BD – C.F.V.S.), and individual Assistant Researcher contracts (2020.00366.CEECIND/CP1589/CT0006, DOI

10.54499/2020.00366.CEECIND/CP1589/CT0006 – S.G.P.; 2020.00758.CEECIND/CP1589/CT0007, DOI 10.54499/2020.00758.CEECIND/CP1589/CT0007 – J.B.) under the Scientific Employment Stimulus – Individual Call, respectively. S.F. thanks FCT for her research contract (REF-069-88-ARH-2018), which is funded by national funds (OE) through FCT, I. P., in the scope of the framework contract foreseen in the numbers 4, 5, and 6 of the article 23, of the Decree-Law 57/ 2016, of August 29, changed by Law 57/2017, of July 19. This work was developed within the scope of the project CICECO-Aveiro Institute of Materials, UIDB/50011/2020 (DOI 10.54499/UIDB/50011/2020), UIDP/50011/2020 (DOI 10.54499/UIDP/50011/2020) & LA/P/0006/2020 (DOI 10.54499/LA/P/0006/2020), financed by national funds through the FCT/MEC (PIDDAC). The authors gratefully acknowledge Dr Hélène L. Lauzon from Primex EHF (Siglufjordur, Iceland) for kindly providing the chitosan batch used in this work.

ABBREVIATIONS

AFM, atomic force microscopy; ATR-FTIR, attenuated total reflectance-Fourier transform infrared spectroscopy; CD, circular dichroism spectroscopy; CHT, chitosan; *d*, interplanar spacing; ECM, extracellular matrix; HDF, primary human adult dermal fibroblast cell line; LbL, layer-by-layer assembly technology; SEM, scanning electron microscopy; SS, silk sericin; QCM-D, quartz crystal microbalance with dissipation monitoring; R_q, root-mean-square surface roughness; WCA, water contact angle; WAXS, powder wide-angle X-ray scattering.

REFERENCES

1. Hussey, G. S.; Dziki, J. L.; Badylak, S. F. Extracellular matrix-based materials for regenerative medicine. *Nat. Rev. Mater.* **2018**, *3*, 159–173. DOI: https://doi.org/10.1038/s41578-018-0023-x.

2. Badylak, S. F. The extracellular matrix as a biologic scaffold material. *Biomaterials* **2007**, *28*, 3587–3593. DOI: https://doi.org/10.1016/j.biomaterials.2007.04.043.

3. Goor, O. J. G. M.; Hendrikse, S. I. S.; Dankers, P. Y. W.; Meijer, E. W. From supramolecular polymers to multi-component biomaterials. *Chem. Soc. Rev.* **2017**, *46*, 6621–6637. DOI: https://doi.org/10.1039/C7CS00564D.

4. Gu, Y.; Zhu, J.; Xue, C.; Li, Z.; Ding, F.; Yang, Y.; Gu, X. Chitosan/silk fibroin-based, Schwann cell-derived extracellular matrix-modified scaffolds for bridging rat sciatic nerve gaps. *Biomaterials* **2014**, *35*, 2253–2263. DOI: https://doi.org/10.1016/j.biomaterials.2013.11.087.

5. Farokhi, M.; Mottaghitalab, F.; Samani, S.; Shokrgozar, M. A.; Kundu, S. C.; Reis, R. L.; Fatahi, Y.; Kaplan, D. L. Silk fibroin/hydroxyapatite composites for bone tissue engineering. *Biotechnol. Adv.* **2018**, *36*, 68–91. DOI: https://doi.org/10.1016/j.biotechadv.2017.10.001.

6. Ebrahimi, D.; Tokareva, O.; Rim, N. G.; Wong, J. Y.; Kaplan, D. L.; Buehler, M. J. Silk–Its Mysteries, How It Is Made, and How It Is Used. *ACS Biomater. Sci. Eng*. **2015**, *1*, 864–876. DOI: https://doi.org/10.1021/acsbiomaterials.5b00152.

7. Murphy, A. R.; Kaplan, D. L. Biomedical applications of chemically-modified silk fibroin. *J. Mater. Chem.* **2009**, *19*, 6443–6450. DOI: DOI https://doi.org/10.1039/B905802H.

8. Sahoo, J. K.; Hasturk, O.; Falcucci, T.; Kaplan, D. L. Silk chemistry and biomedical material designs. *Nat. Rev. Chem.* **2023**, *7*, 302–318. DOI: https://doi.org/10.1038/s41570-023-00486-x.

9. Promsuk, J.; Manissorn, J.; Laomeephol, C.; Luckanagul, J. A.; Methachittipan, A.; Tonsomboon, K.; Jenjob, R.; Yang, S. G.; Thongnuek, P.; Wangkanont, K. Optimizing protein delivery rate from silk fibroin hydrogel using silk fibroin-mimetic peptides conjugation. *Sci. Rep.* **2024**, *14*, 4428. DOI: https://doi.org/10.1038/s41598-024-53689-7.

10. Silva, S. S.; Popa, E. G.; Gomes, M. E.; Oliveira, M. B.; Nayak, S.; Subia, B.; Mano, J. F.; Kundu, S. C.; Reis, R. L. Silk hydrogels from non-mulberry and mulberry silkworm cocoons processed with ionic liquids. *Acta. Biomater.* **2013**, *9*, 8972–8982. DOI. https://doi.org/10.1016/j.actbio.2013.06.044.

11. Fuest, S.; Smeets, R.; Gosau, M.; Aavani, F.; Knipfer, C.; Grust, A. L. C.; Kopp, A.; Becerikli, M.; Behr, B.; Matthies, L. Layer-by-Layer Deposition of Regenerated Silk Fibroin─An Approach to the Surface Coating of Biomedical Implant Materials. *ACS Biomater. Sci. Eng.* **2023**, *9*, 6644–6657. DOI: https://doi.org/10.1021/acsbiomaterials.3c00852.

12. Acharya, C.; Ghosh, S. K.; Kundu, S. C. Silk fibroin film from non-mulberry tropical tasar silkworms: A novel substrate for in vitro fibroblast culture. *Acta Biomater.* **2009**, *5*, 429–437. DOI: https://doi.org/10.1016/j.actbio.2008.07.003.

13. Liu, J.; Xie, X.; Wang, T.; Chen, H.; Fu, Y.; Cheng, X.; Wu, J.; Li, G.; Liu, C.; Liimatainen, H.; Zheng, Z.; Wang, X.; Kaplan, D. L. Promotion of Wound Healing

Using Nanoporous Silk Fibroin Sponges. *ACS Appl. Mater. Interfaces* **2023**, *15*, 12696–12707. DOI: https://doi.org/10.1021/acsami.2c20274.

14. Shchepelina, O.; Drachuk, I.; Gupta, M. K.; Lin, J.; Tsukruk, V. V. Silk-on-Silk Layer-by-Layer Microcapsules. *Adv. Mater.* **2011**, *23*, 4655–4660. DOI: https://doi.org/10.1002/adma.201102234.

15. Fink, T. D.; Zha, R. H. Silk and Silk-Like Supramolecular Materials. *Macromol. Rapid Commun.* **2018**, *39*, 1700834. DOI: https://doi.org/10.1002/marc.201700834.

16. Oliveira, A. L.; Sun, L.; Kim, H. J.; Hu, X.; Rice, W.; Kluge, J.; Reis, R. L.; Kaplan, D. L. Aligned silk-based 3-D architectures for contact guidance in tissue engineering. *Acta Biomater.* **2012**, *8*, 1530–1542. DOI: https://doi.org/10.1016/j.actbio.2011.12.015.

17. Borges, J.; Mano, J. F. Molecular Interactions Driving the Layer-by-Layer Assembly of Multilayers. *Chem. Rev.* **2014**, *114*, 8883–8942. DOI: https://doi.org/10.1021/cr400531v.

18. Richardson, J. J.; Björnmalm, M.; Caruso, F. Technology-driven layer-by-layer assembly of nanofilms. *Science* **2015**, *348*, aaa2491. DOI: https://doi.org/10.1126/science.aaa2491.

19. Decher, G. Fuzzy Nanoassemblies: Toward Layered Polymeric Multicomposite. *Science* **1997**, *277*, 1232–1237. DOI: https://doi.org/10.1126/science.277.5330.1232.

20. Landry, M. J.; Rollet, F. G.; Kennedy, T. E.; Barrett, C. J. Layers and Multilayers of Self-Assembled Polymers: Tunable Engineered Extracellular Matrix Coatings for Neural Cell Growth. *Langmuir* **2018**, *34*, 8709–8730. DOI: https://doi.org/10.1021/acs.langmuir.7b04108.

21. Sousa, C. F. V.; Monteiro, L. P. G.; Rodrigues, J. M. M.; Borges, J.; Mano, J. F. Marine-origin polysaccharides-based free-standing multilayered membranes as sustainable nanoreservoirs for controlled drug delivery. *J. Mater. Chem. B* **2023**, *11*, 6671–6684. DOI: https://doi.org/10.1039/D3TB00796K.

22. Lopes, M.; Torrado, M.; Barth, D.; Santos, S. D.; Sever-Bahcekapili, M.; Tekinay, A. B.; Guler, M. O.; Cleymand, F.; Pêgo, A. P.; Borges, J.; Mano, J. F. Supramolecular presentation of bioinstructive peptides on soft multilayered nanobiomaterials stimulates neurite outgrowth. *Biomater. Sci.* **2023**, *11*, 5012–5024. DOI: https://doi.org/10.1039/D3BM00438D.

23. Boudou, T.; Crouzier, T.; Ren, K.; Blin, G.; Picart, C. Multiple Functionalities of Polyelectrolyte Multilayer Films: New Biomedical Applications. *Adv. Mater.* **2010**, *22*, 441–467. DOI: https://doi.org/10.1002/adma.200901327.

24. Borges, J.; Zeng, J.; Liu, X. Q.; Chang, H.; Monge, C.; Garot, C.; feng Ren, K.; Machillot, P.; Vrana, N. E.; Lavalle, P.; Akagi, T.; Matsusaki, M.; Ji, J.; Akashi, M.; Mano, J. F.; Gribova, V.; Picart, C. Recent Developments in Layer-by-Layer Assembly for Drug Delivery and Tissue Engineering Applications. *Adv. Healthcare Mater.* **2024**, *13*, 2302713. DOI: https://doi.org/10.1002/adhm.202302713.

25. Bi, X.; Li, L.; Mao, Z.; Liu, B.; Yang, L.; He, W.; Fan, Y.; Li, X. The effects of silk layer-by-layer surface modification on the mechanical and structural retention of extracellular matrix scaffolds. *Biomater. Sci.* **2020**, *8*, 4026–4038. DOI: DOI https://doi.org/10.1039/D0BM00448K.

26. Wang, X.; Kim, H. J.; Xu, P.; Matsumoto, A.; Kaplan, D. L. Biomaterial coatings by stepwise deposition of silk fibroin. *Langmuir* **2005**, *21*, 11335–11341. DOI: https://doi.org/10.1021/la051862m.

27. Delezuk, J. A. M.; Pavinatto, A.; Moraes, M. L.; Shimizu, F. M.; Rodrigues, V. C.; Campana-Filho, S. P.; Ribeiro, S. J. L.; Oliveira, O. N. Silk fibroin organization induced by chitosan in layer-by-layer films: Application as a matrix in a biossensor. *Carbohydr. Polym.* **2017**, *155*, 146–151. DOI: https://doi.org/10.1016/j.carbpol.2016.08.060.

28. de Moraes, M. A.; Crouzier, T.; Rubner, M.; Beppu, M. M. Factors Controlling the Deposition of Silk Fibroin Nanofibrils during Layer-by-Layer Assembly. *Biomacromolecules* **2015**, *16*, 97–104. DOI: https://doi.org/10.1021/bm5012135.

29. Nogueira, G. M.; Swiston, A. J.; Beppu, M. M.; Rubner, M. F. Layer-by-Layer Deposited Chitosan/Silk Fibroin Thin Films with Anisotropic Nanofiber Alignment. *Langmuir* **2010**, *26*, 8953–8958. DOI: https://doi.org/10.1021/la904741h.

30. Shen, G.; Hu, X.; Guan, G.; Wang, L. Surface Modification and Characterisation of Silk Fibroin Fabric Produced by the Layer-by-Layer Self-Assembly of Multilayer Alginate/Regenerated Silk Fibroin. *PLoS ONE* **2015**, *10*, e0124811. DOI: https://doi.org/10.1371/journal.pone.0124811.

31. Lamboni, L.; Gauthier, M.; Yang, G.; Wang, Q. Silk sericin: A versatile material for tissue engineering and drug delivery. *Biotechnol. Adv.* **2015**, *33*, 1855–1867. DOI: https://doi.org/10.1016/j.biotechadv.2015.10.014.

32. Ahsan, F.; Ansari, T. M.; Usmani, S.; Bagga, P. An Insight on Silk Protein Sericin: From Processing to Biomedical Application. *Drug. Res.* **2018**, *68*, 317–327. DOI: https://doi.org/10.1055/s-0043-121464.

33. Liu, J.; Shi, L.; Deng, Y.; Zou, M.; Cai, B.; Song, Y.; Wang, Z.; Wang, L. Silk sericin-based materials for biomedical applications. *Biomaterials* **2022**, *287*, 121638. DOI: https://doi.org/10.1016/j.biomaterials.2022.121638.

34. Veiga, A.; Foster, O.; Kaplan, D. L.; Oliveira, A. L. Expanding the boundaries of silk sericin biomaterials in biomedical applications. *J. Mater. Chem. B* **2024**, *12*, 7020–7040. DOI: https://doi.org/10.1039/D4TB00386A.

35. Kundu, S. C.; Dash, B. C.; Dash, R.; Kaplan, D. L. Natural protective glue protein, sericin bioengineered by silkworms: Potential for biomedical and biotechnological applications. *Prog. Polym. Sci.* **2008**, *33*, 998–1012. DOI: https://doi.org/10.1016/j.progpolymsci.2008.08.002.

36. Wang, Z.; Zhang, Y.; Zhang, J.; Huang, L.; Liu, J.; Li, Y.; Zhang, G.; Kundu, S. C.; Wang, L. Exploring natural silk protein sericin for regenerative medicine: an injectable, photoluminescent, cell-adhesive 3D hydrogel. *Sci. Rep.* **2014**, *4*, 7064. DOI: https://doi.org/10.1038/srep07064.

37. Panilaitis, B.; Altman, G. H.; Chen, J.; Jin, H. J.; Karageorgiou, V.; Kaplan, D. L. Macrophage responses to silk. *Biomaterials* **2003**, *24*, 3079–3085. DOI: https://doi.org/10.1016/S0142-9612(03)00158-3.

38. Wang, J.; Liu, H.; Shi, X.; Qin, S.; Liu, J.; Lv, Q.; Liu, J.; Li, Q.; Wang, Z.; Wang, L. Development and Application of an Advanced Biomedical Material-Silk Sericin. *Adv. Mater.* **2024**, *36*, 2311593. DOI: https://doi.org/10.1002/adma.202470178.

39. Zhang, Y. Q. ; Ma, Y. ; Xia, Y. Y.; De Shen, W. ; Mao, J. P. ; Xue, R. Y. Silk sericin–insulin bioconjugates: Synthesis, characterization and biological activity. *J. Control. Release* **2006**, *115*, 307–315. DOI: https://doi.org/10.1016/j.jconrel.2006.08.019.

40. Teramoto, H.; Kameda, T.; Tamada, Y. Preparation of Gel Film from Bombyx mori Silk Sericin and Its Characterization as a Wound Dressing. *Biosci. Biotechnol. Biochem.* **2008**, *72*, 3189–3196. DOI: https://doi.org/10.1271/bbb.80375.

41. Baptista-Silva, S.; Borges, S.; Costa-Pinto, A. R.; Costa, R.; Amorim, M.; Dias, J. R.; Ramos, O.; Alves, P.; Granja, P. L.; Soares, R.; Pintado, M.; Oliveira, A. L. *In Situ* Forming Silk Sericin-Based Hydrogel: A Novel Wound Healing Biomaterial. *ACS Biomater. Sci. Eng.* **2021**, *7*, 1573–1586. DOI: https://doi.org/10.1021/acsbiomaterials.0c01745.

42. Nayak, S.; Dey, S.; Kundu, S. C. Skin Equivalent Tissue-Engineered Construct: Co-Cultured Fibroblasts/ Keratinocytes on 3D Matrices of Sericin Hope Cocoons. *PLoS ONE* **2013**, *8*, e74779. DOI: https://doi.org/10.1371/journal.pone.0074779.

43. Nishida, A.; Yamada, M.; Kanazawa, T.; Takashima, Y.; Ouchi, K.; Okada, H. Sustained-release of protein from biodegradable sericin film, gel and sponge. *Int. J. Pharm.* **2011**, *407*, 44–52. DOI: https://doi.org/10.1016/j.ijpharm.2011.01.006.

44. Zhang, H. P.; Wang, X. Y.; Min, S. J.; Mandal, M.; Yang, M. Y.; Zhu, L. J. Hydroxyapatite/sericin composite film prepared through mineralization of flexible ethanol-treated sericin film with simulated body fluids. *Ceram. Int.* **2014**, *40*, 985–991. DOI: https://doi.org/10.1016/j.ceramint.2013.06.095.

45. Shah, A.; Ali Buabeid, M.; Arafa, E.-S. A.; Hussain, I.; Li, L.; Murtaza, G. The wound healing and antibacterial potential of triple-component nanocomposite (chitosan-silver-sericin) films loaded with moxifloxacin. *Int. J. Pharm.* **2019**, *564*, 22–38. DOI: https://doi.org/10.1016/j.ijpharm.2019.04.046.

46. Nagura, M.; Ohnishi, R.; Gitoh, Y.; Ohkoshi, Y. Structures and physical properties of cross-linked sericin membranes. *J. Insect. Biotechnol. Sericology* **2001**, *70*, 149–153. DOI: https://doi.org/10.11416/jibs2001.70.149.

47. Veiga, A.; Castro, F.; Reis, C.; Sousa, A.; Oliveira, A. L.; Rocha, F. Hydroxyapatite/sericin composites: a simple synthesis route under near-physiological conditions of temperature and pH and preliminary study of the effect of sericin on the biomineralization process. *Mater. Sci. Eng. C* **2020**, *108*, 110400. DOI: https://doi.org/10.1016/j.msec.2019.110400.

48. Cho, K. Y.; Moon, J. Y.; Lee, Y. W.; Lee, K. G.; Yeo, J. H.; Kweon, H. Y.; Kim, K. H.; Cho, C. S. Preparation of self-assembled silk sericin nanoparticles. *Int. J. Biol. Macromol.* **2003**, *32*, 36–42. DOI: https://doi.org/10.1016/S0141-8130(03)00023-0.

49. Wang, F.; Hou, K.; Chen, W.; Wang, Y.; Wang, R.; Tian, C.; Xu, S.; Ji, Y.; Yang, Q.; Zhao, P.; Yu, L.; Lu, Z.; Zhang, H.; Li, F.; Wang, H.; He, B.; Kaplan, D. L.; Xia, Q. Transgenic PDGF-BB/sericin hydrogel supports for cell proliferation and osteogenic differentiation. *Biomater. Sci.* **2020**, *8*, 657–672. DOI: https://doi.org/10.1039/C9BM01478K.

50. Zhang, Y.; Liu, J.; Huang, L.; Wang, Z.; Wang, L. Design and performance of a sericin-alginate interpenetrating network hydrogel for cell and drug delivery. *Sci. Rep.* **2015**, *5*, 12374. DOI: https://doi.org/10.1038/srep12374.

51. Kundu, B.; Kundu, S. C. Silk sericin/polyacrylamide in situ forming hydrogels for dermal reconstruction. *Biomaterials* **2012**, *33*, 7456–7467. DOI : https://doi.org/10.1016/j.biomaterials.2012.06.091.

52. Qi, C.; Liu, J.; Jin, Y.; Xu, L.; Wang, G.; Wang, Z.; Wang, L. Photo-crosslinkable, injectable sericin hydrogel as 3D biomimetic extracellular matrix for minimally invasive repairing cartilage. *Biomaterials* **2018**, *163*, 89–104. DOI: https://doi.org/10.1016/j.biomaterials.2018.02.016.

53. Chen, C.-S.; Zeng, F.; Xiao, X.; Wang, Z.; Li, X.-L.; Tan, R.-W.; Liu, W.-Q.; Zhang, Y.-S.; She, Z.-D.; Li, S.-J. Three-Dimensionally Printed Silk-Sericin-Based Hydrogel Scaffold: A Promising Visualized Dressing Material for Real-Time Monitoring of Wounds. *ACS Appl. Mater. Interfaces* **2018**, *10*, 33879–33890. DOI: https://doi.org/10.1021/acsami.8b10072.

54. Fu, Z.; Li, W.; Wei, J.; Yao, K.; Wang, Y.; Yang, P.; Li, G.; Yang, Y.; Zhang, L. Construction and Biocompatibility Evaluation of Fibroin/Sericin-Based Scaffolds. *ACS Biomater. Sci. Eng.* **2022**, *8*, 1494–1505. DOI: https://doi.org/10.1021/acsbiomaterials.1c01426.

55. Sapru, S.; Das, S.; Mandal, M.; Ghosh, A. K.; Kundu, S. C. Sericin-chitosan-glycosaminoglycans hydrogels incorporated with growth factors for in vitro and in vivo skin repair. *Carbohydr. Polym.* **2021**, *258*, 117717. DOI: https://doi.org/10.1016/j.carbpol.2021.117717.

56. Karahaliloglu, Z.; Kilicay, E.; Denkbas, E. B. Antibacterial chitosan/silk sericin 3D porous scaffolds as a wound dressing material. *Artif. Cells Nanomed. Biotechnol.* **2017**, *45*, 1172–1185. DOI: https://doi.org/10.1080/21691401.2016.1203796.

57. Pankongadisak, P.; Suwantong, O. The potential use of thermosensitive chitosan/silk sericin hydrogels loaded with longan seed extract for bone tissue engineering. *RSC Adv.* **2018**, *8*, 40219–40231. DOI: https://doi.org/10.1039/C8RA07255H.

58. Islam, Md. M.; Shahruzzaman, Md.; Biswas, S.; Nurus Sakib, Md.; Rashid, T. U. Chitosan based bioactive materials in tissue engineering applications-A review. *Bioact. Mater.* **2020**, *5*, 164–183. DOI: https://doi.org/10.1016/j.bioactmat.2020.01.012.

59. Hunter, R. J. Zeta Potential in Colloid Science: Principle and Applications, Academic Press, London, UK, **1988**.

60. Hoogeveen, N. G.; Cohen Stuart, M. A.; Fleer, G. J.; Böhmer, M. R. Formation and stability of multilayers of polyelectrolytes. *Langmuir* **1996**, *12*, 3675–3681. DOI: https://doi.org/10.1021/la951574y.

61. Voinova, M. V.; Rodahl, M.; Jonson, M.; Kasemo, B. Viscoelastic Acoustic Response of Layered Polymer Films at Fluid-Solid Interfaces: Continuum Mechanics Approach. *Phys. Scr.* **1999**, *59*, 391. DOI: https://doi.org/10.1238/Physica.Regular.059a00391.

62. ISO 10993-5/Ed.3 Biological Evaluation of Medical Devices - Part 5: Tests for in Vitro Cytotoxicity. International Organization for Standardization: Switzerland, **2009**.

63. Yang, M.; Shuai, Y.; Zhou, G.; Mandal, N.; Zhu, L.; Mao, C. Tuning molecular weights of *Bombyx mori* (*B. mori*) silk sericin to modify its assembly structures and materials formation. *ACS Appl. Mater. Interfaces* **2014**, *6*, 13782–13789. DOI: https://doi.org/10.1021/am503214g.

64. Tsukada, M.; Komoto, T.; Kawai, T. Conformation of liquid silk sericin. *Polym. J.* **1979**, *11*, 503–504. DOI: https://doi.org/10.1295/polymj.11.503.

65. Matsuo, K.; Namatame, H.; Taniguchi, M.; Gekko, K. Vacuum-Ultraviolet Circular Dichroism Analysis of Glycosaminoglycans by Synchrotron-Radiation Spectroscopy. *Biosci. Biotechnol. Biochem.* **2009**, *73*, 557–561. DOI: https://doi.org/10.1271/bbb.80605.

66. Chen, L.; Hu, J.; Ran, J.; Shen, X.; Tong, H. A novel nanocomposite for bone tissue engineering based on chitosan–silk sericin/hydroxyapatite: biomimetic synthesis and its cytocompatibility. *RSC Adv.* **2015**, *5*, 56410–56422. DOI: https://doi.org/10.1039/C5RA08216A.

67. Yang, H.; Yang, S.; Kong, J.; Dong, A.; Yu, S. Obtaining information about protein secondary structures in aqueous solution using Fourier transform IR spectroscopy. *Nat. Protoc.* **2015**, *10*, 382–396. DOI: https://doi.org/10.1038/nprot.2015.024.

68. Teramoto, H.; Miyazawa, M. Molecular Orientation Behavior of Silk Sericin Film as Revealed by ATR Infrared Spectroscopy. *Biomacromolecules* **2005**, *6*, 2049–2057. DOI. https://doi.org/10.1021/bm0500547.

69. Zhao, R.; Li, X.; Sun, B.; Zhang, Y.; Zhang, D.; Tang, Z.; Chen, X.; Wang, C. Electrospun chitosan/sericin composite nanofibers with antibacterial property as potential wound dressings. *Int. J. Biol. Macromol.* **2014**, *68*, 92–97. DOI: https://doi.org/10.1016/j.ijbiomac.2014.04.029.

70. Borges, J.; Sousa, M. P.; Cinar, G.; Caridade, S. G.; Guler, M. O.; Mano, J. F. Nanoengineering Hybrid Supramolecular Multilayered Biomaterials Using Polysaccharides and Self-Assembling Peptide Amphiphiles. *Adv. Funct. Mater.* **2017**, *27*, 1605122. DOI: https://doi.org/10.1002/adfm.201605122.

71. Caridade, S. G.; Monge, C.; Gilde, F.; Boudou, T.; Mano, J. F.; Picart, C. Free-Standing Polyelectrolyte Membranes Made of Chitosan and Alginate. *Biomacromolecules* **2013**, *14*, 1653–1660. DOI: https://doi.org/10.1021/bm400314s.

72. Geminiani, L.; Campione, F. P.; Corti, C.; Giussani, B.; Gorla, G.; Luraschi, M.; Recchia, S.; Rampazzi, L. Historical silks: a novel method to evaluate their condition

with ATR-FTIR spectroscopy and Principal Component Analysis. *J. Cult. Herit.* **2024**, *67*, 9–22. DOI: https://doi.org/10.1016/j.culher.2024.01.015.

73. Hu, X.; Kaplan, D.; Cebe, P. Determining Beta-Sheet Crystallinity in Fibrous Proteins by Thermal Analysis and Infrared Spectroscopy. *Macromolecules* **2006**, *39*, 6161–6170. DOI: https://doi.org/10.1021/ma0610109.

74. Cai, Y.; Jin, J.; Mei, D.; Xia, N.; Yao, J. Effect of silk sericin on assembly of hydroxyapatite nanocrystals into enamel prism-like structure. *J. Mater. Chem.* **2009**, *19*, 5751–5758. DOI: https://doi.org/10.1039/B901620A.

75. Banik, N.; Hussain, A.; Ramteke, A.; Sharma, H. K.; Maji, T. K. Preparation and evaluation of the effect of particle size on the properties of chitosan-montmorillonite nanoparticles loaded with isoniazid. *RSC Adv.* **2012**, *2*, 10519–10528. DOI: https://doi.org/10.1039/C2RA20702H.

76. Mukhopadhyay, P.; Sarkar, K.; Soam, S.; Kundu, P. P. Formulation of pH-responsive carboxymethyl chitosan and alginate beads for the oral delivery of insulin. *J. Appl. Polym. Sci.* **2013**, *129*, 835–845. DOI: https://doi.org/10.1002/app.38814.

77. Cheng, P.-N.; Pham, J. D.; Nowick, J. S. The Supramolecular Chemistry of β-Sheets. *J. Am. Chem. Soc.* **2013**, *135*, 5477–5492. DOI: https://doi.org/10.1021/ja3088407.

78. Marx, K. A. Quartz Crystal Microbalance: A Useful Tool for Studying Thin Polymer Films and Complex Biomolecular Systems at the Solution−Surface Interface. *Biomacromolecules* **2003**, *4*, 1099–1120. DOI: https://doi.org/10.1021/bm020116i.

79. Pujana, M. A.; Pérez-Álvarez, L.; Iturbe, L. C. C.; Katime, I. Water dispersible pH-responsive chitosan nanogels modified with biocompatible crosslinking-agents. *Polymer* **2012**, *53*, 3107–3116. DOI: https://doi.org/10.1016/j.polymer.2012.05.027.

80. Ogino, M.; Tanaka, R.; Hattori, M.; Yoshida, T.; Yokote, Y.; Takanashi, K. Interfacial Behavior of Fatty-Acylated Sericin Prepared by Lipase-Catalyzed Solid-Phase Synthesis. *Biosci. Biotechnol. Biochem.* **2006**, *70*, 66–75. DOI: https://doi.org/10.1271/bbb.70.66.

81. Schwinté, P.; Ball, V.; Szalontai, B.; Haikel, Y.; Voegel, J.-C.; Schaaf, P. Secondary Structure of Proteins Adsorbed onto or Embedded in Polyelectrolyte Multilayers. *Biomacromolecules* **2002**, *3*, 1135–1143. DOI: https://doi.org/10.1021/bm025547f.

82. Cardoso, M. J.; Caridade, S. G.; Costa, R. R.; Mano, J. F. Enzymatic Degradation of Polysaccharide-Based Layer-by-Layer Structures. *Biomacromolecules* **2016**, *17*, 1347–1357. DOI: https://doi.org/10.1021/acs.biomac.5b01742.

83. Easley, A. D.; Ma, T.; Eneh, C. I.; Yun, J.; Thakur, R. M.; Lutkenhaus, J. L. A practical guide to quartz crystal microbalance with dissipation monitoring of thin polymer films. *J. Polym. Sci.* **2022**, *60*, 1090–1107. DOI: https://doi.org/10.1002/pol.20210324.

84. Rousseau, M. E.; Lefèvre, T. ; Beaulieu, L. ; Asakura, T. ; Pézolet, M. Study of Protein Conformation and Orientation in Silkworm and Spider Silk Fibers Using Raman Microspectroscopy. *Biomacromolecules* **2004**, *5*, 2247–2257. DOI : https://doi.org/10.1021/bm049717v.

85. Pavoni, E.; Tsukada, M.; Taddei, P. Influence of grafting with acrylate compounds on the conformational rearrangements of silk fibroin upon electrospinning and treatment with aqueous methanol. *J. Raman Spectrosc.* **2016**, *47*, 1367–1374. DOI: https://doi.org/10.1002/jrs.4974.

86. Lefèvre, T. ; Rousseau, M.-E.; Pézolet, M. Protein Secondary Structure and Orientation in Silk as Revealed by Raman Spectromicroscopy. *Biophys. J.* **2007**, *92*, 2885–2895. DOI: https://doi.org/10.1529/biophysj.106.100339.

87. Nirmala, R.; Il, B. W.; Navamathavan, R.; El-Newehy, M. H.; Kim, H. Y. Preparation and characterizations of anisotropic chitosan nanofibers via electrospinning. *Macromol. Res.* **2011**, *19*, 345–350. DOI: https://doi.org/10.1007/s13233-011-0402-2.

88. Khire, T. S.; Kundu, J.; Kundu, S. C.; Yadavalli, V. K. The fractal self-assembly of the silk protein sericin. *Soft Matter* **2010**, *6*, 2066–2071. DOI: https://doi.org/10.1039/B924530H.

89. Kamble, S.; Agrawal, S.; Cherumukkil, S.; Sharma, V.; Jasra, R. V.; Munshi, P. Revisiting Zeta Potential, the Key Feature of Interfacial Phenomena, with Applications and Recent Advancements. *ChemistrySelect* **2022**, *7*, e202103084. DOI: https://doi.org/10.1002/SLCT.202103084.

90. Kumar, S.; Chauhan, N.; Gopal, M.; Kumar, R.; Dilbaghi, N. Development and evaluation of alginate–chitosan nanocapsules for controlled release of acetamiprid. *Int. J. Biol. Macromol.* **2015**, *81*, 631–637. DOI: https://doi.org/10.1016/j.ijbiomac.2015.08.062.

For Table of Contents Use Only

Silk Sericin/Chitosan Supramolecular Multilayered Thin Films as Sustainable Cytocompatible Nanobiomaterials

Miguel Rosas,[1,2] Cristiana F. V. Sousa,[1] Ana Pereira,[1] Adérito J. R. Amaral,[1] Tamagno Pesqueira,[1] Sónia G. Patrício,[1] Sara Fateixa,[1] Helena I. S. Nogueira,[1] João F. Mano,[1] Ana L. Oliveira,[2*] and João Borges[1*]

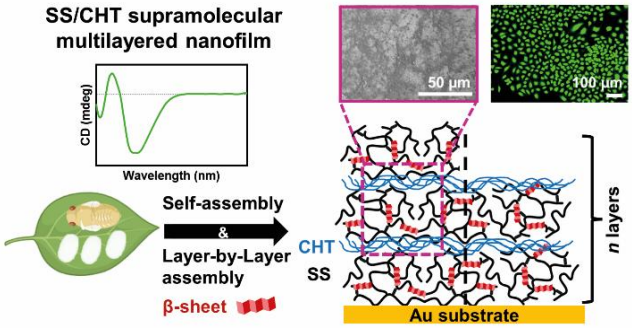

Author manuscript of article published in *Biomacromolecules* **2024**. DOI: 10.1021/acs.biomac.4c01146

Supporting Information

Silk Sericin/Chitosan Supramolecular Multilayered Thin Films as Sustainable Cytocompatible Nanobiomaterials

Miguel Rosas,[1,2] Cristiana F. V. Sousa,[1] Ana Pereira,[1] Adérito J. R. Amaral,[1] Tamagno Pesqueira,[1] Sónia G. Patrício,[1] Sara Fateixa,[1] Helena I. S. Nogueira,[1] João F. Mano,[1] Ana L. Oliveira,[2] and João Borges[1*]*

[1]CICECO – Aveiro Institute of Materials, Department of Chemistry, University of Aveiro, Campus Universitário de Santiago, 3810-193 Aveiro, Portugal

[2]CBQF-Centro de Biotecnologia e Química Fina – Laboratório Associado, Universidade Católica Portuguesa, Escola Superior de Biotecnologia, Rua Diogo Botelho 1327, 4169-005 Porto, Portugal

* Corresponding authors: aloliveira@ucp.pt (A.L.O.), joaoborges@ua.pt (J.B.)

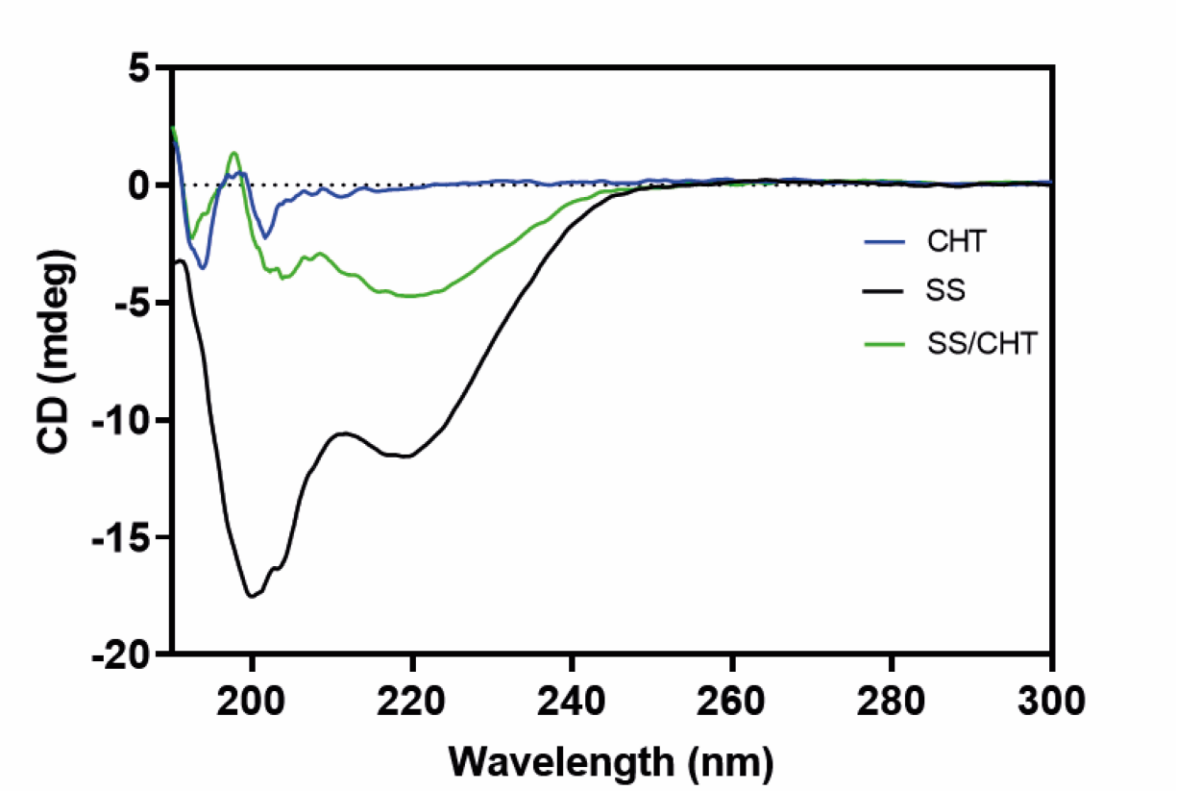

Figure S1. CD spectra of the individual components (SS and CHT) and co-assembled system (SS/CHT, 0.9:1 v/v) at pH 5.5.

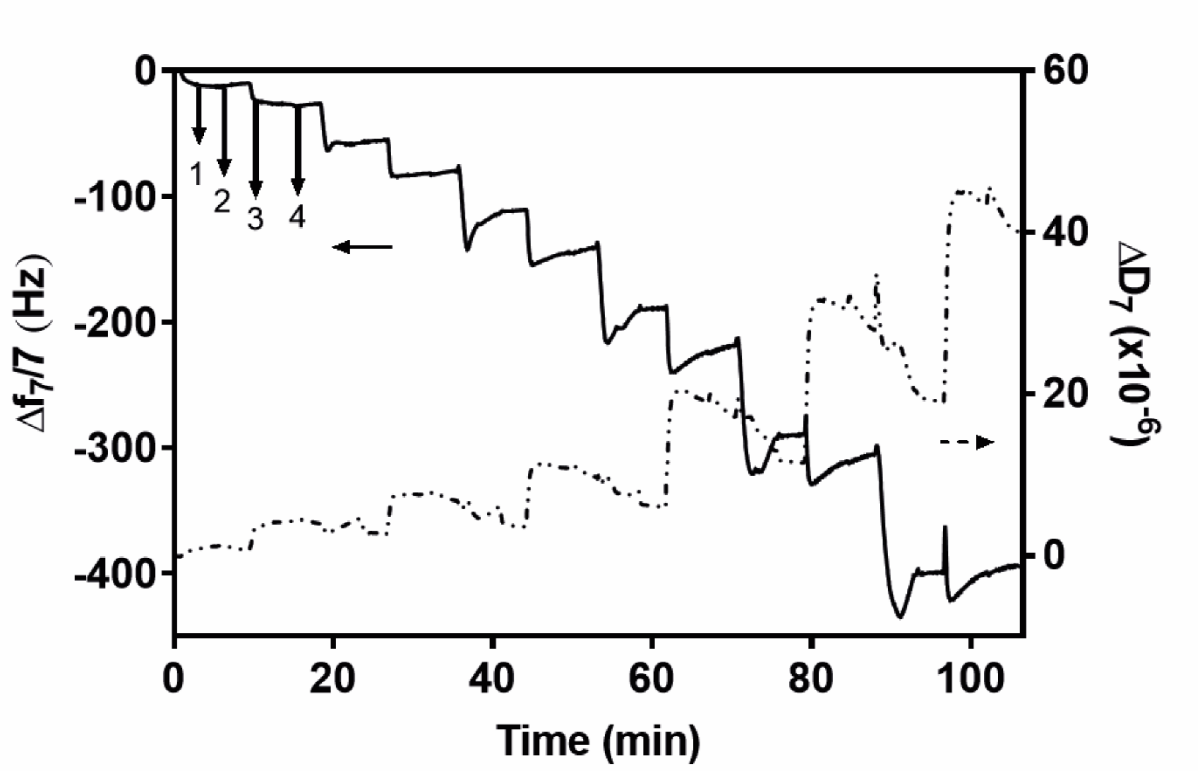

Figure S2. QCM-D monitoring of the normalized frequency ($\Delta f_n/n$, straight line) and dissipation (ΔD_n, dashed line) shifts, obtained at the seventh overtone (n = 7; 35 MHz), as a function of time, for the build-up of the $(SS/CHT)_6$ supramolecular multilayered thin film at pH 5.5 onto Au-coated quartz crystal sensors and intermediate rinsing steps. The inset numbers refer to the adsorption of SS (1), CHT (3), and rinsing steps (2 and 4).

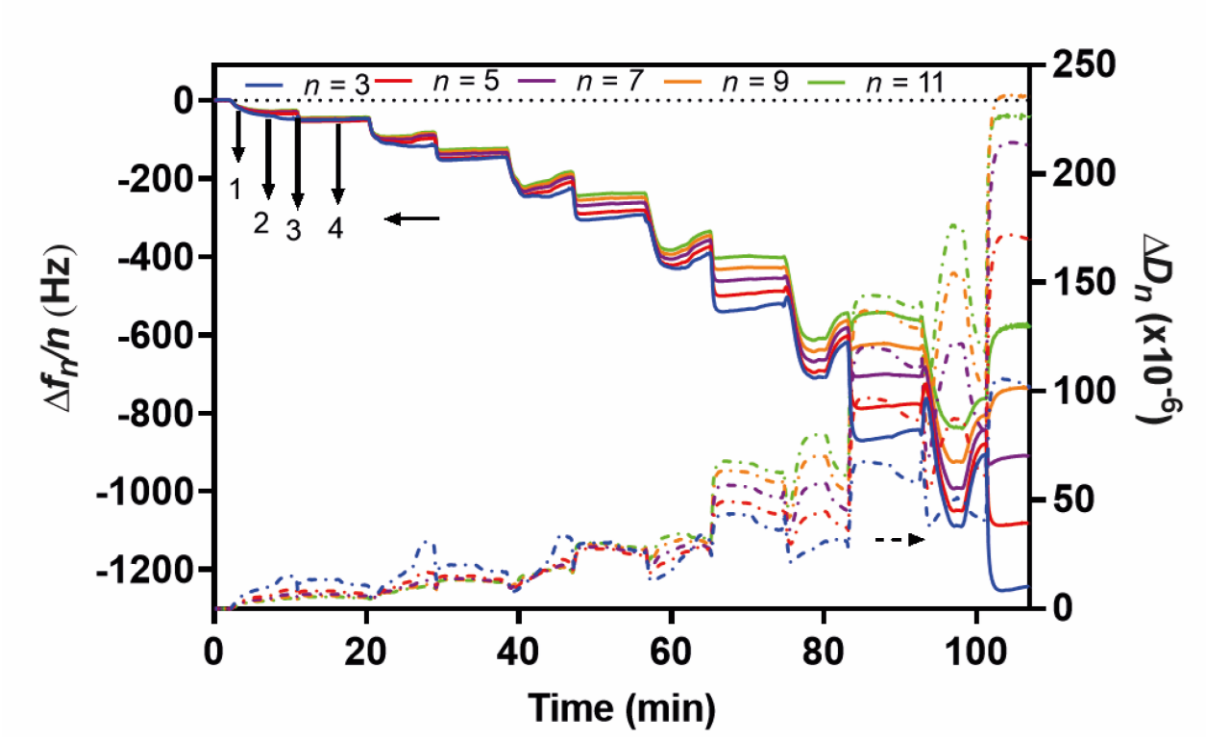

Figure S3. QCM-D monitoring of the normalized frequency ($\Delta f_n/n$, straight lines) and dissipation (ΔD_n, dashed lines) shifts, obtained at the 3rd overtone (n = 3; 15 MHz), 5th overtone (n = 5; 25 MHz), 7th overtone (n = 7; 35 MHz), 9th overtone (n = 9; 45 MHz), and 11th overtone (n = 11; 55 MHz), as a function of time, for the build-up of the $(SS/CHT)_6$ supramolecular multilayered thin film (SS assembled at pH 7, CHT assembled at pH 5.5) onto Au-coated quartz crystal sensors and intermediate rinsing steps. The inset numbers refer to the adsorption of SS (1), CHT (3), and rinsing steps (2 and 4).

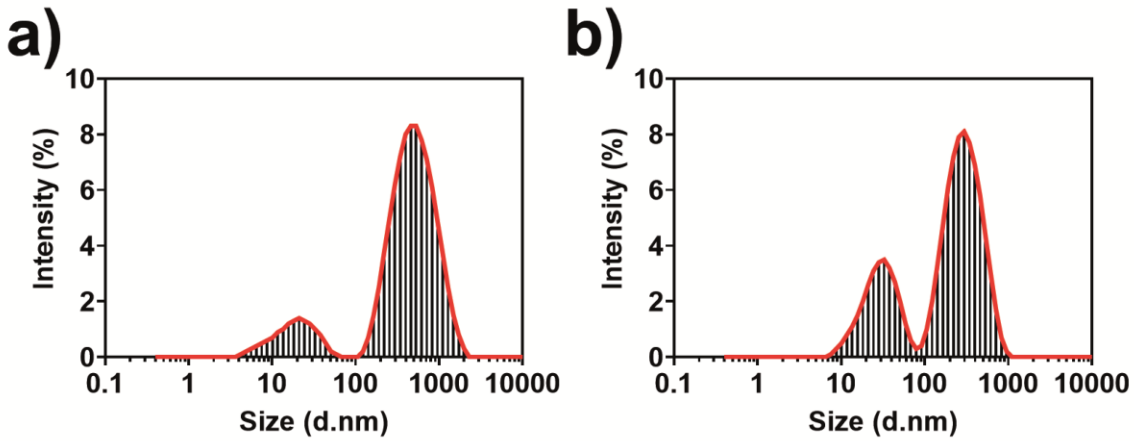

Figure S4. Particles' size distribution of the (a) SS and (b) CHT aqueous solutions measured via DLS.